

ENERGY SOURCES AND LIGHT CURVES OF MACRONOVAE

SHOTA KISAKA¹, KUNIHITO IOKA^{1,2}, AND HAJIME TAKAMI^{1,3}

draft v1

ABSTRACT

A macronova (kilonova) was discovered with short gamma-ray burst, GRB 130603B, which is widely believed to be powered by the radioactivity of r -process elements synthesized in the ejecta of a neutron star binary merger. As an alternative, we propose that macronovae are energized by the central engine, i.e., a black hole or neutron star, and the injected energy is emitted after the adiabatic expansion of ejecta. This engine model is motivated by extended emission of short GRBs. In order to compare the theoretical models with observations, we analytically formulate the light curves of macronovae. The engine model allows a wider parameter range, especially smaller ejecta mass, and better fit to observations than the r -process model. Future observations of electromagnetic counterparts of gravitational waves should distinguish energy sources and constrain the activity of central engine and r -process nucleosynthesis.

Subject headings: — —

1. INTRODUCTION

Gravitational wave (GW) observations are expected to provide a new view of relativistic phenomena in the Universe. One of the most promising candidates for the direct detection of GWs is the merger of compact binaries such as binary neutron stars (NSs). The second generation of ground-based GW detectors, such as Advanced LIGO (Abadie et al. 2010a), Advanced VIRGO (Acernese et al. 2014) and KAGRA (Kuroda et al. 2010), will reach the sensitivity required to detect GWs from the inspiral and coalescence of compact binary systems including binary NSs within a few hundred Mpc. Statistical studies suggest that a few tens of merger events should be observed per year (Abadie et al. 2010b).

Electromagnetic counterparts of GW emitters have been recently focused on to maximize a scientific return from the expected detection of GWs (e.g., Metzger & Berger (2012)). Follow-up observations of these electromagnetic counterparts are important to confirm a GW detection and to investigate progenitors and environments. The electromagnetic detection also improves the localization of GW sources because the localization accuracy by photons is much better than that by the ground-based GW detectors $\sim 10 - 100 \text{ deg}^2$ (e.g., Essick et al. (2014)).

Sophisticated simulations have revealed mass ejection associated with the mergers of binary NSs by several mechanisms. Significant mass is dynamically ejected by gravitational torques and hydrodynamical interactions during the mergers, called dynamical ejecta (e.g., Rosswog et al. (1999); Ruffert & Janka (2001); Hotokezaka et al. (2013a)). General rela-

tivistic simulations show that these ejecta distribute nearly isotropic compared to Newtonian simulations in the cases of binary NSs (Hotokezaka et al. 2013a), while they are anisotropic for NS-black hole (BH) mergers (Kyutoku, Ioka & Shibata 2013). Mass may be also ejected through winds driven by neutrinos (Dessart et al. 2009), magnetic fields of and/or amplified by the merged objects (Shibata et al. 2011; Kiuchi, Kyutoku & Shibata 2012; Kiuchi et al. 2014), viscous heating and nuclear recombination (Fernández & Metzger 2013; Fernández et al. 2014).

A traditional electromagnetic counterpart is short-hard gamma-ray bursts (GRBs; Narayan, Paczyński & Piran (1992)). Recent simulations have revealed that a hypermassive NS is formed from the merger of a NS binary (e.g., Hotokezaka et al. (2013a)), which is believed to collapse into a BH at later time. Non-collapsed matter and some ejecta falling back to the BH form a torus around the BH (e.g., Rosswog (2007)). Then, a relativistic jet may be launched from the BH-torus system, which is believed to be the central engine of short-hard GRBs. Another interesting possibility is a so-called macronova/kilonova, which is thermal emission from ejecta (e.g., Li & Paczyński (1998); Kulkarni (2005); Barnes & Kasen (2013)). The radiative energy of a macronova is estimated between that of a classical nova and supernova. Ejecta can also produce non-thermal emission at later time similarly to supernova remnants (Nakar & Piran 2011; Piran, Nakar & Rosswog 2013; Takami, Kyutoku & Ioka 2014). Ejecta may accompany a relativistic outer part and produce early emission (Kyutoku, Ioka & Shibata 2014; Metzger et al. 2014). Emission from macronovae and NS binary merger remnants is almost isotropic and hence different from that of short GRBs which depend on the directions of their relativistic jets. Moreover, macronovae are closer in time to mergers than emission from merger remnants and do not depend on the properties of circumstellar environments. Therefore, macronovae are expected to play a crucial role to localize a large sample of GW

kisaka@post.kek.jp
kunihiro.ioka@kek.jp
takami@post.kek.jp

¹ Theory Center, Institute of Particle and Nuclear Studies, KEK, Tsukuba 305-0801, Japan

² Department of Particle and Nuclear Physics, the Graduate University for Advanced Studies (Sokendai), Tsukuba 305-0801, Japan

³ JSPS Research Fellow

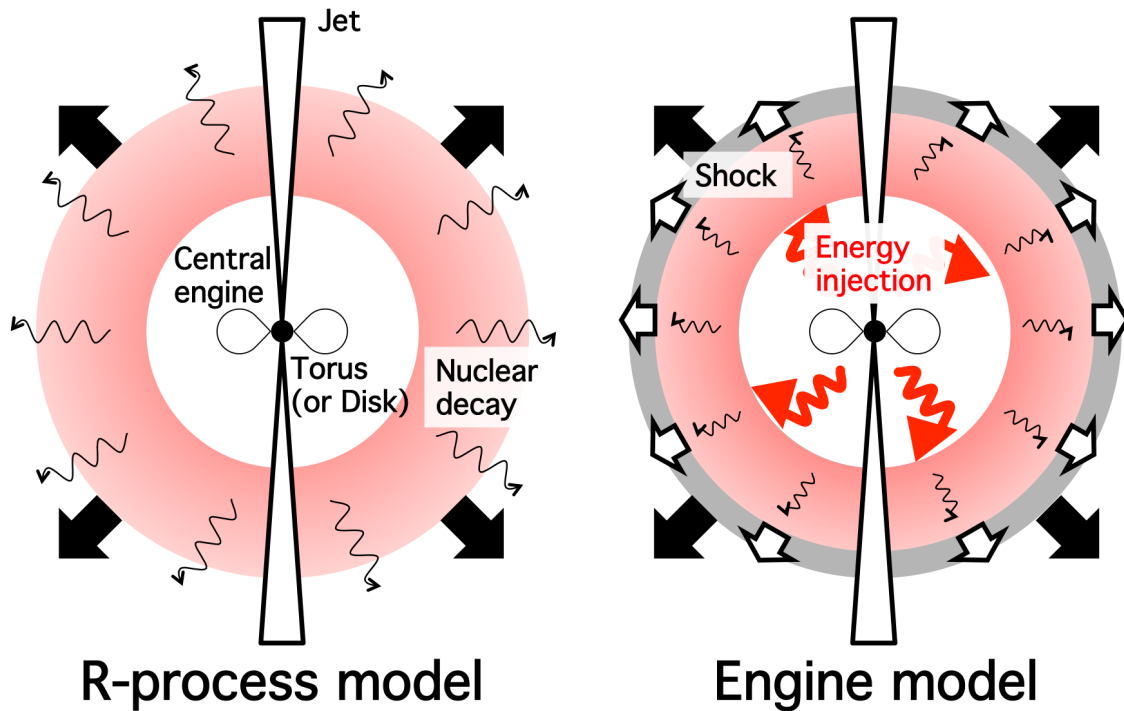


FIG. 1.— Schematic pictures for the r -process model (left) and the engine model (right).

events (Metzger & Berger 2012).

Recently, a macronova candidate following GRB 130603B was discovered (Tanvir et al. 2013; Berger, Fong & Chornock 2013). This candidate is widely interpreted as the results of the radioactive decay of r -process elements produced in the ejecta of a compact binary merger (Tanvir et al. 2013; Berger, Fong & Chornock 2013; Hotokezaka et al. 2013b; Piran, Korobkin & Rosswog 2014; Grossman et al. 2014). We call this scenario *an r-process model* throughout this paper. The ejecta from a merger of binary NSs is primarily neutron-rich. Then, heavy radioactive elements (mass number $\gtrsim 130$) are expected to form through neutron-capture onto nuclei (r -process nucleosynthesis) (e.g., Lattimer & Schramm (1974)). Although the r -process nucleosynthesis ends a few hundred millisecond after a merger, synthesized elements release energy due to nuclear fission and beta decays up to ~ 100 days (e.g., Wanajo et al. (2014)). A schematic picture for this model is shown in the left panel of figure 1. If this scenario is correct, the observations also give important insights into the enrichment of r -process elements in the galaxy evolution (e.g., Piran, Korobkin & Rosswog (2014)). Although the r -process model explains the observed light curve of the macronova, it is based on the limited observational data and the nuclear heating rate with large uncertainties. Required mass of dynamical ejecta to explain the observations is relatively large compared with the simulation results (Grossman et al. 2014). In addition, the occurrence of r -process nucleosynthesis needs the ejecta with

low electron fraction ($Y_e \lesssim 0.1$). However, relatively high electron fraction ($Y_e \sim 0.2 - 0.5$) can be also realized, which has been discussed for neutrino-driven wind (e.g., Fernández & Metzger (2013)). It is worth considering other possibilities such as the scenarios of an external shock between ejecta and surrounding medium (Jin et al. 2013), a supramassive magnetar (Fan et al. 2013) and dust grains (Takami, Nozawa & Ioka 2014).

In this study, we consider another power source of macronovae, i.e., energy injection from the activity of the central engine, in addition to the radioactive decay of r -process elements. We call this model *an engine model* throughout this paper. There are several motivations to consider that the activity of the central engine contributes to the heating of ejecta. One observational motivation is an extended emission following the prompt emission of short GRBs. The origin of extended emission is considered to be the activity of the central engine (Barthelmy et al. 2005) because the sharp drop of its light curve is difficult to be reproduced by afterglow emission (Ioka, Kobayashi & Zhang 2005). After the merger, a stable NS or a BH is formed. In the case that a BH with a torus (or disk) is formed, the energy injection to the ejecta is expected as a form of the jet and/or disk wind (e.g., Nakamura et al. (2013)). In the case that a NS with strong poloidal magnetic field is formed as a result of a merger, the wind of relativistic particles is ejected. Then, the kinetic-energy-dominated wind collides with the ejecta, and about half of the kinetic energy converts to the internal energy by the shock-heating. A schematic picture is shown in the right-hand side of figure 1.

The engine model can provide energy enough to reproduce the detected macronova candidate, GRB 130603B. To estimate the luminosity and temperature, we assume that the internal energy $E_{\text{int}0} \sim 10^{51}$ erg is injected to the ejecta at the time $t_{\text{inj}} \sim 10^2$ s after the merger. These values are consistent with typical isotropic energy $E_{\text{iso}} \sim 10^{50} - 10^{51}$ erg and duration $t_{\text{dur}} \sim 10 - 10^2$ s of the extended emission (Sakamoto et al. 2011). Using the velocity of the ejecta v , the temperature at t_{inj} is $T_0 \sim [E_{\text{int}0}/(av^3t_{\text{inj}}^3)]^{1/4}$, where a is the radiative constant. If we only consider the adiabatic cooling for the cooling process of the ejecta, the evolution of the internal energy E_{int} and temperature T is scaled as $E_{\text{int}} \propto t^{-1}$ and $T \propto t^{-1}$. The luminosity is described as $L \sim E_{\text{int}}/t$. Adopting the ejecta velocity $v \sim 10^{10}$ cm s $^{-1}$ (Hotokezaka et al. 2013a), the luminosity L and the temperature T at $t \sim 10^6$ s are

$$L \sim \frac{E_{\text{int}0}}{t} \left(\frac{t}{t_{\text{inj}}} \right)^{-1} \sim 10^{41} \left(\frac{E_{\text{int}0}}{10^{51} \text{erg}} \right) \left(\frac{t_{\text{inj}}}{10^2 \text{s}} \right) \left(\frac{t}{10^6 \text{s}} \right)^{-2} \text{erg s}^{-1}, \quad (1)$$

and

$$T \sim T_0 \left(\frac{t}{t_{\text{inj}}} \right)^{-1} \sim 2 \times 10^3 \left(\frac{E_{\text{int}0}}{10^{51} \text{erg}} \right)^{1/4} \left(\frac{t_{\text{inj}}}{10^2 \text{s}} \right)^{1/4} \times \left(\frac{v}{10^{10} \text{cm s}^{-1}} \right)^{-3/4} \left(\frac{t}{10^6 \text{s}} \right)^{-1} \text{K}. \quad (2)$$

The observations of macronova of GRB 130603B give J-band luminosity $\sim 10^{41}$ erg s $^{-1}$ and the difference between J-band and B-band $\gtrsim 2.5$ mag which corresponds to the temperature $\lesssim 4 \times 10^3$ K at $t \sim 7$ days after GRB 130603B in the source rest frame (Tanvir et al. 2013). Therefore, in this estimate, the luminosity and temperature for the engine model is consistent with the observation of the macronova following GRB130603B.

We model the evolution of luminosity and temperature of a macronova. Unlike the previous studies, we treat the model in an analytical manner and formulate a light curve including the early phase ($\sim 10^3 - 10^5$ s), which is important for the search of electromagnetic counterparts of GW emitters. We consider shock-heating due to the activity of a central engine as a heating mechanism of the ejecta. For comparison, the r -process model, which has been discussed in most papers (e.g., Li & Paczyński (1998)), is also formulated. Then, we compare the results of our models with observations to constrain the model parameters such as the ejected mass and the velocity of the ejecta. Although our models are simplified, it is valuable to use the comparison between two heating models. In section 2, we introduce our model assumptions. We describe the analytical model for the evolution of luminosity and temperature in section 3. Then, we compare our results with the observations in section 4. Implications for the discrimination between two models are also discussed. We summarize our results in section 5. In appendix A, we summarize the formula for the observed temperature and bolometric luminosity.

2. MODEL

Significant mass of material $\sim 10^{-3} - 10^{-1} M_{\odot}$ is ejected during a binary merger. We model ejecta by following the results of the general relativistic simulations of NS-NS mergers in Hotokezaka et al. (2013a). The simulations show that ejecta expand in a nearly homologous manner (see also Rosswog et al. (2014)). The morphology of the ejecta is quasi-spherical in the case of a merger of binary NSs. According to these results, we assume an isotropic and homologous expansion for the ejecta. Then, the velocity of ejecta v is

$$v \sim r/t \quad (3)$$

where the radius r originates the central engine and the time t is measured from the time when a compact binary merges.

Note that in the case of a merger of NS-BH binary, the ejected mass expands with significant anisotropy (Kyutoku et al. 2011; Foucart et al. 2013, 2014; Lovelace et al. 2013; Deaton et al. 2013; Kyutoku, Ioka & Shibata 2013). We do not consider such anisotropic ejecta in this work.

2.1. Density Profile

Nagakura et al. (2014) found that the profile of ejecta obtained from simulations by Hotokezaka et al. (2013a) can be well fitted by a power-law function $\rho \propto v^{-\beta}$. The power-law index of snapshot density β is more or less independent on the dynamics of mergers, which is in the range of $\beta \sim 3-4$ for $v_{\text{min}} \leq v \leq v_{\text{max}}$, where v_{max} and v_{min} are the velocities of the outer and inner edges of the ejecta, respectively. We choose the middle of this range $\beta = 3.5$ in this study. We also fix the maximum velocity $v_{\text{max}} = 0.4c$ from simulation results (Hotokezaka et al. 2013a). The maximum velocity v_{max} is comparable with the escape velocity of the system. The minimum velocity v_{min} is mainly determined by complicated dynamics at the initial stage of the merger $t \ll 10^2$ s. Here, we only consider the evolution after this time ($t \gg t_{\text{inj}}$) and treat v_{min} as a model parameter. Because of homologous expansion, the density decreases as $\rho \propto t^{-3}$. Then the density profile is described by

$$\rho(t, v) = \rho_0 \left(\frac{t}{t_0} \right)^{-3} \left(\frac{v}{v_{\text{min}}} \right)^{-\beta}. \quad (4)$$

where ρ_0 and t_0 are normalization factors. The factor $\rho_0 t_0^3$ is related to the total mass of the ejecta M_{ej} as following,

$$M_{\text{ej}} = 4\pi \int_{v_{\text{min}} t_0}^{v_{\text{max}} t_0} \rho(t_0, v) r^2 dr = \frac{4\pi}{\beta - 3} \rho_0 (v_{\text{min}} t_0)^3 \left[1 - \left(\frac{v_{\text{max}}}{v_{\text{min}}} \right)^{3-\beta} \right], \quad (5)$$

where we use $dr(t = t_0) = t_0 dv$ from equation (3). We also introduce the radius of ejecta outer edge

$$r_{\text{out}} = v_{\text{max}} t, \quad (6)$$

and its inner edge

$$r_{\text{in}} = v_{\text{min}} t. \quad (7)$$

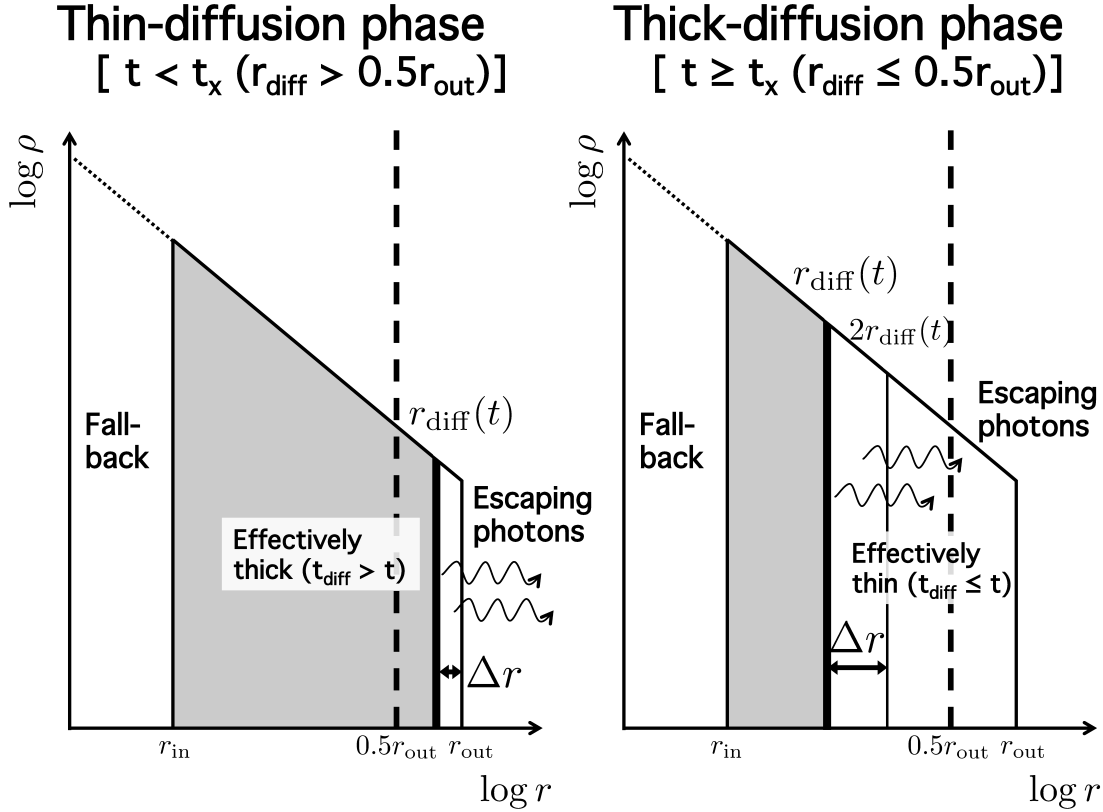


FIG. 2.— Schematic pictures for the thin- (left) and thick-diffusion phases (right). The horizontal and vertical axes show the radius which originates the central engine and the mass density of the ejecta in logarithmic scales, respectively. The radii r_{out} and r_{in} correspond to the outer and inner edges of the ejecta. Ejecta expand in a homologous manner ($v \sim r/t$). Materials at the inner edge of the ejecta (dotted line) are considered to fall back to the central engine. The thick vertical lines show the diffusion radius r_{diff} in which the diffusion time equals to the dynamical time. Photons emitted from the right side of the thick vertical line (effectively thin region) can diffuse out from the ejecta. The effectively thick region corresponds to the shaded area. The size Δr is the propagation distance to evaluate the diffusion time. Since most scatterings occur near the diffusion radius, we divide two phases whether the diffusion radius is larger than $0.5r_{\text{out}}$ (thick vertical dashed lines) or not. The time t_x corresponds to the time when the diffusion radius equals to the half of the radius of the outer edge of the ejecta. See text for details.

2.2. Diffusion Radius

An inner part of the ejecta is optically thick, and therefore the propagation of radiation in the ejecta can be regarded as a diffusion process. Photons can diffusively escape from the region which satisfies that the diffusion time, t_{diff} , is smaller than the dynamical time t ,

$$t_{\text{diff}} \leq t. \quad (8)$$

The medium in this region is called to be effectively thin (Rybicki & Lightman 1979). For convenience, we introduce a diffusion radius $r_{\text{diff}}(t)$ which is the radius satisfying the condition $t = t_{\text{diff}}$. Furthermore, we divide ejecta into two regions called the effectively thin ($r \geq r_{\text{diff}}$) and effectively thick ($r < r_{\text{diff}}$) regions. Near the diffusion radius, the optical depth is $\tau \gg 1$. We consider random walk for photons so that the mean number of scatterings to propagate for the distance Δr is $(\Delta r/l_{\text{mfp}})^2$, where l_{mfp} is the mean free path for a photon. Hence, the diffusion time t_{diff} for the propagation distance Δr is

$$t_{\text{diff}} \sim \frac{l_{\text{mfp}}}{c} \left(\frac{\Delta r}{l_{\text{mfp}}} \right)^2 \sim \tau \frac{\Delta r}{c}. \quad (9)$$

In the right hand of equation (9), we use $\tau \sim \Delta r/l_{\text{mfp}}$.

We calculate the diffusion radius r_{diff} from the condition $t_{\text{diff}} = t$. Since the mass density profile of the ejecta is described by a decreasing power-law function (equation 4), the diffusion time t_{diff} is negligible at an outer part. Thus, in order to calculate the diffusion radius r_{diff} , it is a good approximation to only consider scatterings near r_{diff} ($\Delta r \sim r_{\text{diff}}$). However, in the early phase, the distance from the outer edge of the ejecta r_{out} to the diffusion radius r_{diff} is smaller than the diffusion radius $r_{\text{out}} - r_{\text{diff}} < r_{\text{diff}}$. Therefore, we should take the propagation distance as

$$\Delta r \sim \begin{cases} r_{\text{out}} - r_{\text{diff}} & (r_{\text{diff}} > 0.5r_{\text{out}}) \\ r_{\text{diff}} & (r_{\text{diff}} \leq 0.5r_{\text{out}}). \end{cases} \quad (10)$$

We call the first the thin-diffusion phase and the second the thick-diffusion phase throughout this paper. We schematically show these two phases in figure 2. Note that in the thin-diffusion phase, since the size of the effectively thin region is much smaller than the size of the ejecta ($r_{\text{out}} - r_{\text{in}}$), the calculation of the radiative transfer using Monte Carlo technique (e.g., Barnes & Kasen (2013); Tanaka & Hotokezaka (2013)) requires a large number of cells to follow the temporal evolution.

To obtain the diffusion radius, we need to calculate the optical depth τ of photons which propagate a distance Δr . Using equations (4) and (10), the optical depth τ is described as,

$$\begin{aligned}\tau &= \int_{r_{\text{diff}}}^{r_{\text{out}}} \kappa \rho dr \\ &= \frac{(\beta - 3)\kappa M_{\text{ej}}}{4\pi(\beta - 1)v_{\text{min}}^2 t^2} \left[1 - \left(\frac{v_{\text{max}}}{v_{\text{min}}} \right)^{3-\beta} \right]^{-1} \\ &\quad \times \left[\left(\frac{r_{\text{diff}}}{v_{\text{min}} t} \right)^{1-\beta} - \left(\frac{v_{\text{max}}}{v_{\text{min}}} \right)^{1-\beta} \right],\end{aligned}\quad (11)$$

in the thin-diffusion phase, and

$$\begin{aligned}\tau &= \int_{r_{\text{diff}}}^{2r_{\text{diff}}} \kappa \rho dr \\ &= \frac{(\beta - 3)\kappa M_{\text{ej}}}{4\pi(\beta - 1)v_{\text{min}}^2 t^2} \left[1 - \left(\frac{v_{\text{max}}}{v_{\text{min}}} \right)^{3-\beta} \right]^{-1} \\ &\quad \times \left(\frac{r_{\text{diff}}}{v_{\text{min}} t} \right)^{1-\beta} (1 - 2^{1-\beta}),\end{aligned}\quad (12)$$

in the thick-diffusion phase, where κ is the opacity of the ejecta. For simplicity, we use grey approximation and a spatially uniform value of the opacity κ . From the results of Tanaka & Hotokezaka (2013) (see also Kasen, Badnell & Barnes (2013)) which consider the contribution from all r -process elements to the opacity of merger ejecta, the evolution of the bolometric luminosity can be approximately described by the constant value of the opacity, $\kappa \sim 3 - 30 \text{ cm}^2 \text{g}^{-1}$. Following their results, we use this value for the opacity of the ejecta. Note that the exact value of the opacity of the ejecta has some uncertainties such as the production efficiency of r -process elements and its spatial distribution. Moreover, if the ejecta temperature is low enough for dust formation ($T \lesssim 2000 \text{ K}$), the opacity significantly increases (Takami, Nozawa & Ioka 2014). From these reasons, we consider the dependence of κ in section 3.

2.3. Heating Mechanisms

2.3.1. Radioactivity

One of the two heating mechanisms we consider is nuclear heating by r -process elements. Since the beta decay products of r -process elements produced in NS binary mergers naturally heat ejecta, this mechanism is considered to power the emission of a macronova (e.g., Li & Paczyński (1998)). The nuclear heating rate is calculated in several works (Metzger et al. 2010; Roberts et al. 2011; Korobkin et al. 2012; Rosswog et al. 2014; Wanajo et al. 2014). The derived heating rates per unit mass $\dot{\epsilon}(t)$ are described by the following formula

$$\dot{\epsilon} = \dot{\epsilon}_0 \left(\frac{t}{1 \text{ day}} \right)^{-\alpha}. \quad (13)$$

In this study, we use $\alpha = 1.3$ and $\dot{\epsilon}_0 = 2 \times 10^{10} \text{ erg s}^{-1} \text{g}^{-1}$ obtained by Wanajo et al. (2014). The value of $\dot{\epsilon}$ has

been obtained by simulations under some simplified assumptions with only limited parameter regions. Thus, we should note that the value of $\dot{\epsilon}_0$ has uncertainties.

The injected internal energy by the nuclear decay is $\propto t^{1-\alpha}$ in the region $r < r_{\text{diff}}$. On the other hand, the injected energy in this region is decreased by adiabatic cooling. The time-evolution of internal energy due to the adiabatic cooling is proportional to t^{-1} . Comparing the two temporal evolution, the index of the adiabatic cooling is smaller than that of the increase of internal energy due to the nuclear decay for $\alpha < 2$. Since we use $\alpha = 1.3$, we neglect the injected internal energy in the region $r < r_{\text{diff}}$.

2.3.2. Engine-driven shock

Unlike the r -process model, energy injection occurs only within the time t_{inj} in the engine model. We only consider adiabatic cooling as a cooling process of ejecta after t_{inj} , and therefore, the temperature distribution at time t is,

$$T(t, v) = T_0 \left(\frac{t}{t_{\text{inj}}} \right)^{-1} \left(\frac{v}{v_{\text{min}}} \right)^{-\xi}, \quad (14)$$

where the index ξ is a parameter for a snapshot distribution and T_0 is a normalization factor described later. The time dependence of t^{-1} is the effect of adiabatic expansion.

The normalized value T_0 is determined by using the relation of total injected internal energy E_{int0} as

$$\begin{aligned}E_{\text{int0}} &= 4\pi \int_{v_{\text{min}} t_{\text{inj}}}^{v_{\text{max}} t_{\text{inj}}} a T^4(t_{\text{inj}}, v) r^2 dr \\ &= \frac{4\pi}{3 - 4\xi} a T_0^4 (v_{\text{min}} t_{\text{inj}})^3 \left[\left(\frac{v_{\text{max}}}{v_{\text{min}}} \right)^{3-4\xi} - 1 \right] \quad (15)\end{aligned}$$

where we use $dr = t_{\text{inj}} dv$. For the temperature index $\xi > 0.75$, the innermost region of ejecta has dominant internal energy. As will be shown in Section 3, since the luminosity and temperature always depend on the product of E_{int0} and t_{inj} , we treat $E_{\text{int0}} t_{\text{inj}}$ as a parameter. Thus, the engine model has two parameters, ξ and $E_{\text{int0}} t_{\text{inj}}$ instead of $\dot{\epsilon}_0$ and α in the r -process model.

Energy injection is not always a single event and the shock does not always get through the whole part of the ejecta. It is considered that the activity of the central engine accompanies violent time variability. In this case, multiple shocks propagate into the ejecta. Some of the shock may not catch up with the outer edge of the ejecta. Current general relativistic simulations cannot calculate such a long time after merger ($t_{\text{inj}} \sim 10^2 \text{ s}$), so that the index ξ of temperature distribution is highly uncertain. Therefore, we use the temperature index ξ as a parameter.

Unlike the case of core-collapse supernova (Nakar & Sari 2010), it is difficult to determine the temperature distribution of heated ejecta by the activity of a central engine. In the case that the activity of a central engine injects the energy into the ejecta, the radiation-dominated shock (i.e., the internal energy behind the shock is dominated by radiation) is formed in the ejecta. The ejecta are heated during the propagation of the shock. This situation is similar to the initial

phase of core-collapse supernovae (e.g., Arnett (1980); Popov (1993)). In the cases of core-collapse supernovae, the kinetic energy of ejecta before the shock heating is much smaller than the injected internal energy. In such ejecta, the relation between velocity and mass density was obtained by Sakurai (1960) (in non-relativistic case for the velocity of the ejecta). Using Sakurai's (1960) solution and the equipartition between the kinetic energy after the shock heating and the internal energy (Nakar & Sari 2010), the distribution of the temperature distribution is derived. However, in the case of compact binary mergers, the merger ejecta have a large velocity ($\sim 0.01 - 0.1c$) before the shock heating (Hotokezaka et al. 2013a). Then, injected internal energy is not always larger than the kinetic energy of ejecta so that it is not clear that we can use the equipartition to estimate the distribution of internal energy.

The kinetic energy of the ejecta E_{kin} is described as

$$E_{\text{kin}} = \frac{1}{2} 4\pi \int_{v_{\text{min}}}^{v_{\text{max}}} \rho(t, v) v^4 t^3 dv$$

$$= \frac{1}{2} M_{\text{ej}} v_{\text{min}}^2 \frac{(\beta - 3) \left[\left(\frac{v_{\text{max}}}{v_{\text{min}}} \right)^{5-\beta} - 1 \right]}{(5 - \beta) \left[1 - \left(\frac{v_{\text{max}}}{v_{\text{min}}} \right)^{3-\beta} \right]}. \quad (16)$$

Note that if the injected internal energy E_{int0} is larger than the kinetic energy of the ejecta, it is expected that some of internal energy convert to the kinetic energy of the ejecta so that two energies are equally divided as the case of core-collapse supernovae. Then, the mass density distribution, the maximum velocity of the ejecta derived from simulations may be changed because the injection time may be long $\sim 10^2$ s compared to that calculated by simulations $\lesssim 0.1$ s (Hotokezaka et al. 2013a). For simplicity, we only consider the case $E_{\text{int0}} \leq E_{\text{kin}}$.

3. EVOLUTION OF LUMINOSITIES AND TEMPERATURES

In this section, we present the evolution of the observed temperature and luminosity of a macronova using our model introduced in previous section. In sections 3.1 – 3.3, we focus on the parameter dependence of the evolution using some approximations. In section 3.4, we calculate the temperature and luminosity using the fiducial model with parameters summarized in the first column of table 1.

To calculate the luminosity and temperature, we assume that the emission is well described by the blackbody radiation (e.g., Barnes & Kasen (2013)). For simplicity, we assume that the observed temperature equals to the temperature at the diffusion radius r_{diff} . We also assume that the temperature is not so different from the diffusion radius r_{diff} to $2r_{\text{diff}}$ so that in the thick-diffusion phase ($r_{\text{out}} > 2r_{\text{diff}}$), we only consider the emission from r_{diff} to $2r_{\text{diff}}$ to calculate the observed luminosity for both the r -process and engine models. In some studies (e.g., Metzger et al. (2014)), the observed temperature is approximated by the temperature at the radius of the photosphere r_{ph} where the optical depth is unity. Since the velocity of the ejecta is near the light speed, the optical depths at the diffusion radius r_{diff} and its twice $2r_{\text{diff}}$ are $\tau \sim 1 - 10^2$. Therefore, our assumed temperature

approximately equals to the temperature at the photosphere.

In section 2.2, we introduce two phases, the thin- and thick-diffusion phases (figure 2), depending on the size of the region where photons make the diffusion in the ejecta Δr . We also introduce another phase $r_{\text{diff}} \leq r_{\text{in}}$, the transparent phase, in which photons can diffuse out from the entire of the ejecta. Thus, we divide the evolution into these three phases for the values of the diffusion radius r_{diff} as described below.

3.1. Thin-diffusion phase

The size of the effectively thin region gets larger with time. At the early phase of a macronova, the diffusion radius r_{diff} , the inner radius of the effectively thin region, is near the outer edge of the ejecta r_{out} . In this early phase, we should take the propagation distance Δr of a photon as $\Delta r \sim r_{\text{out}} - r_{\text{diff}} (< r_{\text{diff}})$. Since we assume that the density is a homologous function of the velocity $\rho \propto v^{-\beta}$, the density can be approximated as $\rho \sim \rho(v_{\text{max}})$ in the region $r_{\text{diff}} \gg \Delta r$. Using the escaping condition for the diffusing photons $t \sim t_{\text{diff}}$, equation (9) and approximation on the optical depth $\tau \sim \Delta r \kappa \rho(t, v_{\text{max}})$, the propagation distance Δr can be estimated as

$$\Delta r \sim \sqrt{\frac{ct}{\kappa \rho(t, v_{\text{max}})}}$$

$$\propto \kappa^{-1/2} M_{\text{ej}}^{-1/2} v_{\text{min}}^{\frac{3-\beta}{2}} v_{\text{max}}^{\beta/2} t^2. \quad (17)$$

In the discussion of parameter dependence (sections 3.1 – 3.3), we only consider the dominant term. For example, we neglect the second term in the right-hand side of equation (5) to derive the parameter equation (17) because the index of the mass density is $\beta > 3$ in our model. In section 3.4, we include the subdominant terms to calculate the light curves.

First we consider the r -process model. The evolution of temperature T_{obs} is obtained by the internal energy density $\dot{e}\rho$ at the radius $r = r_{\text{out}}$. Using equations (4) and (5), the parameter dependence of the density is $\rho(t, v_{\text{max}}) \propto M_{\text{ej}} v_{\text{min}}^{\beta-3} v_{\text{max}}^{-\beta} t^{-3}$. The observed temperature is

$$T_{\text{obs}} \sim \left(\frac{\dot{e}\rho(t, v_{\text{max}})}{a} \right)^{1/4}$$

$$\propto M_{\text{ej}}^{1/4} v_{\text{min}}^{\frac{\beta-3}{4}} v_{\text{max}}^{-\beta/4} t^{-\frac{2+\alpha}{4}}. \quad (18)$$

For $\alpha = 1.3$, the observed temperature evolves as $T_{\text{obs}} \propto t^{-0.875}$. This is because in the thin-diffusion phase the ejecta is effectively one expanding shell with $\rho \sim \rho(t, v_{\text{max}})$ and the injected energy $\dot{e}t \propto t^{-0.3}$ is almost constant so that the observed temperature approximately follow adiabatic cooling $T \propto t^{-1}$. Note that in this phase the observed temperature does not depend on the opacity. The bolometric luminosity L_{bol} for the radioactivity is described as the product of the mass within the thickness Δr in equation (17) and the nuclear heating rate \dot{e} in equation (13) so that

$$L_{\text{bol}} \sim 4\pi r_{\text{out}}^2 \Delta r \rho(t, v_{\text{max}}) \dot{e}$$

$$\propto \kappa^{-1/2} M_{\text{ej}}^{1/2} v_{\text{min}}^{\frac{\beta-3}{2}} v_{\text{max}}^{\frac{4-\beta}{2}} t^{1-\alpha}. \quad (19)$$

TABLE 1 Model parameters.

Symbol		Fudicial model	Minimum mass model	Hot interior model
M_{ej}	Ejecta mass	$0.10M_{\odot}$	$0.022M_{\odot}$	$0.08M_{\odot}$
v_{min}	Minimum velocity	$0.15c$	$0.13c$	$0.18c$
v_{max}	Maximum velocity	$0.40c$	$0.40c$	$0.40c$
β	Index of the density profile	3.5	3.5	3.5
κ	Opacity	$10 \text{ cm}^2 \text{ g}^{-1}$	$30 \text{ cm}^2 \text{ g}^{-1}$	$10 \text{ cm}^2 \text{ g}^{-1}$
$\dot{\epsilon}_0$	Nuclear heating rate at 1 day	$2 \times 10^{10} \text{ erg s}^{-1} \text{ g}^{-1}$	\dots	$2 \times 10^{10} \text{ erg s}^{-1} \text{ g}^{-1}$
α	Index of nuclear heating rate	1.3	\dots	1.3
$E_{\text{int}0}$	Internal energy at t_{inj}	$1.3 \times 10^{51} \text{ erg}$	$0.9 \times 10^{51} \text{ erg}$	$0.8 \times 10^{51} \text{ erg}$
t_{inj}	Injection time	10^2 s	10^2 s	10^2 s
ξ	Index of the temperature profile	1.6	1.1	2.7

For $\alpha = 1.3$, the evolution of the bolometric luminosity is $L_{\text{bol}} \propto t^{-0.3}$.

Next we consider the engine model. We should take into account the freedom of the temperature index ξ in the temperature distribution (equation 14). Since we only consider a dominant term in the right-hand side of equation (15) (the first term for $\xi < 0.75$ or the second term for $\xi > 0.75$) in this subsection, the parameter dependence of the temperature T_0 is described as

$$T_0 \propto E_{\text{int}0}^{1/4} t_{\text{inj}}^{-3/4} \times \begin{cases} v_{\text{min}}^{-\xi} v_{\text{max}}^{\frac{4\xi-3}{4}} & (\xi < 0.75) \\ v_{\text{min}}^{-3/4} & (\xi > 0.75) \end{cases}. \quad (20)$$

Substituting $v = v_{\text{max}}$ into equation (14), the observed temperature is described as

$$T_{\text{obs}} \sim T_0 \left(\frac{t}{t_{\text{inj}}} \right)^{-1} \left(\frac{v_{\text{max}}}{v_{\text{min}}} \right)^{-\xi} \propto E_{\text{int}0}^{1/4} t_{\text{inj}}^{1/4} t^{-1} \times \begin{cases} v_{\text{max}}^{-3/4} & (\xi < 0.75) \\ v_{\text{min}}^{\frac{4\xi-3}{4}} v_{\text{max}}^{-\xi} & (\xi > 0.75). \end{cases} \quad (21)$$

Since the observed temperature T_{obs} approximately equals to the temperature at the outer edge of the ejecta, $T_{\text{obs}} \sim T(t, v_{\text{max}})$, the evolution of the observed temperature and the luminosity are also determined by the adiabatic cooling. The bolometric luminosity in the effectively thin region is equal to the total radiation created by thermal emission in this region (Rybicki & Lightman 1979). Using equation (21), the bolometric luminosity is described as

$$L_{\text{bol}} \sim 4\pi r_{\text{out}}^2 \Delta r \frac{aT_{\text{obs}}^4}{t} \propto \kappa^{-1/2} M_{\text{ej}}^{-1/2} E_{\text{int}0} t_{\text{inj}} t^{-1} \times \begin{cases} v_{\text{min}}^{\frac{3-\beta}{2}} v_{\text{max}}^{\frac{\beta-2}{2}} & (\xi < 0.75) \\ v_{\text{min}}^{\frac{-3-\beta+8\xi}{2}} v_{\text{max}}^{\frac{4+\beta-8\xi}{2}} & (\xi > 0.75). \end{cases} \quad (22)$$

The time evolution of bolometric luminosity in the engine model does not depend on the temperature index ξ .

Comparing the engine model with the r -process model in the thin-diffusion phase, the bolometric luminosity and the observed temperature decrease faster in the engine model than those in the r -process model. These time-dependence do not depend on the indices of the density and temperature.

Note that in this thin-diffusion phase, the light curve may depend on the detailed profile of the front of the ejecta. The profile of the ejecta front is difficult to calculate by the numerical simulation due to its low density, and hence has large uncertain (Kyutoku, Ioka & Shibata 2014). We discuss its dependence in section 4.

3.2. Thick-diffusion phase

We consider the diffusion near the diffusion radius r_{diff} to evaluate the diffusion radius in the thick-diffusion phase. We take the propagation distance $\Delta r \sim r_{\text{diff}}$ after the time when the difference between the radius of the outer edge of the ejecta r_{out} and the diffusion radius r_{diff} is larger than the diffusion radius, $r_{\text{out}} - r_{\text{diff}} > r_{\text{diff}}$. In this thick-diffusion phase, mass density significantly deviates from $\rho(v_{\text{max}})$. We have to consider the density profile (equation 4). Substituting equations (9) and (12) into $t = t_{\text{diff}}$, the diffusion radius r_{diff} is calculated as

$$r_{\text{diff}} \sim \left[\frac{(\beta-3)\kappa M_{\text{ej}} v_{\text{min}}^{\beta-3} t^{\beta-4}}{4\pi(\beta-1)c} \right]^{\frac{1}{\beta-2}} \propto \kappa^{\frac{1}{\beta-2}} M_{\text{ej}}^{\frac{1}{\beta-2}} v_{\text{min}}^{\frac{\beta-3}{\beta-2}} t^{\frac{\beta-4}{\beta-2}}, \quad (23)$$

where we use the relations $\Delta r \sim r_{\text{diff}}$ and $v \sim r_{\text{diff}}/t$. The latter is obtained from the assumption of the homologous expansion. For the optical depth τ , we neglect the second term in the right-hand side of equation (11) because we only focus on the parameter dependence in sections 3.1 – 3.3. After section 3.4, we do not neglect this subdominant term. For $\beta = 3.5$, the diffusion radius decreases with time ($r_{\text{diff}} \propto t^{-1/3}$). Then, emission from the region with relatively high mass density can be observed progressively in this phase ($\rho \propto t^{-3}(r_{\text{diff}}/t)^{-\beta} \propto t^{(4\beta-9)/3} = t^{1.667}$).

We introduce the transition time t_{\times} between thin- and thick-diffusion phases, which satisfies the relation $r_{\text{diff}} = 0.5r_{\text{out}}$. Substituting equation (23) and $r_{\text{out}} = v_{\text{max}}t$ into the relation $r_{\text{diff}} = 0.5r_{\text{out}}$, we can obtain the transition time t_{\times} as

$$t_{\times} \sim \sqrt{\frac{2^{\beta-4}(\beta-3)\kappa M_{\text{ej}}}{\pi(\beta-1)cv_{\text{max}}} \left(\frac{v_{\text{max}}}{v_{\text{min}}} \right)^{3-\beta}} \sim 4.1 \kappa_{10}^{1/2} M_{\text{ej},0.1}^{1/2} v_{\text{min},0.1}^{\frac{\beta-3}{2}} v_{\text{max},0.4}^{\frac{2-\beta}{2}} \text{ day}, \quad (24)$$

where $\kappa_{10} \equiv \kappa/10 \text{ cm}^2 \text{ g}^{-1}$, $M_{\text{ej},0.1} \equiv M_{\text{ej}}/0.1M_{\odot}$, $v_{\text{min},0.1} \equiv v_{\text{min}}/0.1c$ and $v_{\text{max},0.4} \equiv v_{\text{max}}/0.4c$. As seen

above, the transition time t_\times is typically several days. This timescale is expected to allow the follow-up observations (Aasi et al. 2014). Thus, we should consider both phases to predict something useful for follow-up observations. If we fix κ and v_{\max} and use $\beta = 3.5$, equation (24) gives $t_\times \propto M_{\text{ej}}^{1/2} v_{\min}^{1/4}$. The increases of total mass of the ejecta M_{ej} and the velocity at the inner edge of the ejecta v_{\min} increase the mass density of the ejecta ρ so that the optical depth is increased. As a result, the transition time t_\times becomes large.

First, we consider the r -process model. Here, we introduce the velocity $v_{\text{diff}} = r_{\text{diff}}/t$ based on the homologous relation. Using the velocity v_{diff} and equation (23) for the mass density (equation 4), the evolution of temperature is

$$T_{\text{obs}} \sim \left(\frac{\dot{\epsilon} \rho(t, v_{\text{diff}})}{a} \right)^{1/4} \propto \kappa^{\frac{\beta}{4(2-\beta)}} M_{\text{ej}}^{\frac{1}{2(2-\beta)}} v_{\min}^{\frac{\beta-3}{2(2-\beta)}} t^{\frac{1}{\beta-2} - \frac{\alpha}{4}}. \quad (25)$$

For $\alpha = 1.3$ and $\beta = 3.5$, the evolution is described by $T_{\text{obs}} \propto t^{0.341}$ so that the observed temperature increases with time. The bolometric luminosity is described as the product of the mass between r_{diff} and $2r_{\text{diff}}$ and the nuclear heating rate $\dot{\epsilon}$. Using equations (13) and (23), we obtain the bolometric luminosity as,

$$L_{\text{bol}} \sim 4\pi r_{\text{diff}}^3 \rho(t, v_{\text{diff}}) \dot{\epsilon} \propto \kappa^{\frac{3-\beta}{4(2-\beta)}} M_{\text{ej}}^{\frac{1}{2(2-\beta)}} v_{\min}^{\frac{\beta-3}{2(2-\beta)}} t^{\frac{2(\beta-3)}{\beta-2} - \alpha}. \quad (26)$$

For $\alpha = 1.3$ and $\beta = 3.5$, the evolution of the bolometric luminosity is $L_{\text{bol}} \propto t^{-0.633}$.

Next, we consider the engine model. Using equations (14) and (23), the evolution of the observed temperature is described as

$$T_{\text{obs}} \sim T_0 \left(\frac{t}{t_{\text{inj}}} \right)^{-1} \left(\frac{v_{\text{diff}}}{v_{\min}} \right)^{-\xi} \propto \kappa^{-\frac{\xi}{\beta-2}} M_{\text{ej}}^{-\frac{\xi}{\beta-2}} E_{\text{int}0}^{1/4} t_{\text{inj}}^{1/4} t^{\frac{-\beta+2\xi+2}{\beta-2}} \times \begin{cases} v_{\min}^{\frac{\xi(\beta-3)}{2-\beta}} v_{\max}^{\frac{4\xi-3}{4}} & (\xi < 0.75) \\ v_{\min}^{\frac{3\beta-6-4\xi}{4(2-\beta)}} & (\xi > 0.75). \end{cases} \quad (27)$$

For $\beta = 3.5$, the value $\xi = 0.75$ is the boundary whether the observed temperature increases with time ($\xi > 0.75$) or not ($\xi < 0.75$). The evolution of the luminosity equals to the total radiation created by thermal emission in the sphere with radius r_{diff} . Using the relation $v(r_{\text{diff}}) \sim r_{\text{diff}}/t$ and equations (23) and (27), we obtain

$$L_{\text{bol}} \sim 4\pi r_{\text{diff}}^3 \frac{a T_{\text{obs}}^4}{t} \propto \kappa^{\frac{3-4\xi}{\beta-2}} M_{\text{ej}}^{\frac{3-4\xi}{\beta-2}} E_{\text{int}0} t_{\text{inj}} t^{\frac{2(\beta+1-4\xi)}{2-\beta}} \times \begin{cases} v_{\min}^{\frac{(3-4\xi)(\beta-3)}{\beta-2}} v_{\max}^{4\xi-3} & (\xi < 0.75) \\ v_{\min}^{\frac{3-4\xi}{2-\beta}} & (\xi > 0.75). \end{cases} \quad (28)$$

If we take $\beta = 3.5$ and $\xi = 1.0$, the evolution of the

bolometric luminosity is $L_{\text{bol}} \propto t^{-0.666}$. This is almost the same dependence as in the r -process model. Note that even if the inner part of the ejecta has the larger internal energy ($\xi > 0.75$), the bolometric luminosity does not always increase with time. Using the relation $E_{\text{int}}(v, t) \propto t^{-1}$, from the adiabatic cooling, the evolution of bolometric luminosity for a given mass shell with v is $L_{\text{bol}} \sim E_{\text{int}}(v) t^{-1} \propto t^{-2}$, where $E_{\text{int}}(v, t)$ is the total internal energy for the mass shell with a given expanding velocity v . Since $E_{\text{int}}(v_{\text{diff}}) \propto v^{3-4\xi}$ and $v_{\text{diff}} = r_{\text{diff}}/t \propto t^{\frac{2}{2-\beta}}$, the bolometric luminosity increases with time for the value of the temperature index $\xi > (\beta+1)/4 = 1.125$.

3.3. Transparent phase

Once the diffusion radius reaches the inner edge of the ejecta ($r_{\text{diff}} = r_{\text{in}}$), all photons emitted from the ejecta can diffuse out within dynamical timescale. If energy is not injected into the ejecta in this transparent phase, the internal energy in the ejecta runs out immediately. The transition time from the thick-diffusion phase to the transparent phase t_{tr} is described as

$$t_{\text{tr}} \sim \sqrt{\frac{(\beta-3)\kappa M_{\text{ej}}}{4\pi(\beta-1)cv_{\min}}} \sim 6.9 \kappa_{10}^{1/2} M_{\text{ej},0.1}^{1/2} v_{\min,0.1}^{-1/2} \text{ day}, \quad (29)$$

where we use the diffusion radius $r_{\text{diff}} = r_{\text{in}}$.

First we consider the r -process model. The observed temperature equals to the temperature at the inner edge of the ejecta, $T_{\text{obs}} \sim [\dot{\epsilon} \rho(v_{\min})/a]^{1/4}$. Using equation (4), we obtain

$$T_{\text{obs}} \sim \left(\frac{\dot{\epsilon} \rho(t, v_{\min})}{a} \right)^{1/4} \propto M_{\text{ej}}^{1/4} v_{\min}^{-3/4} t^{-\frac{2+\alpha}{4}}. \quad (30)$$

Since the energy is continuously injected due to the nuclear heating in the r -process model, the bolometric luminosity from entire ejecta is described as $L_{\text{bol}} \sim M_{\text{ej}} \dot{\epsilon}$. However, the outer part of the ejecta emits photons with lower temperature and/or X-rays and γ -rays produced directly in radioactive decays. Although such emission contributes to the bolometric luminosity, we here only focus on the optical and infrared bands. In the thick-diffusion phase, the observed emission comes from the region between $\sim r_{\text{diff}}$ and $\sim 2r_{\text{diff}}$. In the transparent phase, we assume that the time evolution of the diffusion radius r_{diff} is the same as the thick-diffusion phase until $2r_{\text{diff}} = r_{\text{in}}$ and the observed luminosity comes from the region from r_{in} to $2r_{\text{diff}}$ for simplicity. Then, the bolometric luminosity is described as

$$L_{\text{bol}} \sim 4\pi r_{\text{in}}^3 \rho(t, v_{\min}) \dot{\epsilon} \propto M_{\text{ej}} t^{-\alpha}. \quad (31)$$

Although it appears that this time evolution directly reflects the nuclear decay rate, when we calculate the mass between r_{in} and $2r_{\text{diff}}$ the evolution of the upper limit of the integration $2r_{\text{diff}}$ makes the decrease of the luminosity faster than $\propto t^{-\alpha}$ (see a dashed line in the middle panel of figure 3). In addition, the evolution of r_{diff} depends on the index β (see equation 23) so that the mass between r_{in} and $2r_{\text{diff}}$ also depends on the index β .

Next we consider the engine model. We assume that the internal energy is exhausted when the diffusion radius reaches $2r_{\text{diff}} = r_{\text{in}}$. For the observed temperature T_{obs} , we assume the relation $T_{\text{obs}} = T(t, v_{\text{min}})$ and use equation (14),

$$T_{\text{obs}} \sim T_0 \left(\frac{t}{t_{\text{inj}}} \right)^{-1} \propto E_{\text{int}0}^{1/4} t_{\text{inj}}^{1/4} t^{-1} \times \begin{cases} v_{\text{min}}^{-\xi} v_{\text{max}}^{4\xi-3} & (\xi < 0.75) \\ v_{\text{min}}^{-3/4} & (\xi > 0.75). \end{cases} \quad (32)$$

The bolometric luminosity is described as

$$L_{\text{bol}} \sim 4\pi \int_{r_{\text{in}}}^{2r_{\text{diff}}} \frac{dT_{\text{obs}}^4}{t} \propto E_{\text{int}0} t_{\text{inj}} t^{-2} \times \begin{cases} \kappa^{\frac{3-4\xi}{\beta-2}} M_{\text{ej}}^{\frac{3-4\xi}{\beta-2}} v_{\text{min}}^{\frac{(\beta-3)(3-4\xi)}{\beta-2}} \times v_{\text{max}}^{4\xi-3} t^{\frac{2(3-4\xi)}{2-\beta}} & (\xi < 0.75) \\ 1 & (\xi > 0.75). \end{cases} \quad (33)$$

Since the internal energy at the innermost region almost equals to the total internal energy $E_{\text{int}}(v_{\text{min}}) \sim E_{\text{int}0}(t/t_{\text{inj}})^{-1}$ and determines the bolometric luminosity $L_{\text{bol}} \sim E_{\text{int}}(v_{\text{min}})/t$ for the temperature index $\xi > 0.75$, the bolometric luminosity does not depend on the mass M_{ej} and velocities v_{max} and v_{min} . This luminosity always corresponds to the maximum luminosity for $\xi > 0.75$ so that we can impose the lower limit on the parameter $E_{\text{int}0} t_{\text{inj}}$.

3.4. Fiducial Model

We show the temporal evolution of the diffusion radius r_{diff} , the bolometric luminosity L_{bol} and the observed temperature T_{obs} in figure 3 under the fiducial parameter set. Here, we do not use approximations $\rho(v) \sim \rho(v_{\text{max}})$ and $T(v) \sim T(v_{\text{max}})$ at the thin-diffusion phase as in section 3.1. Instead, the diffusion radius r_{diff} is calculated from equations (9) – (11) without approximations. Using the obtained diffusion radius r_{diff} and the relation $v_{\text{diff}} = r_{\text{diff}}/t$, we calculate the observed temperatures in the thin- and thick-diffusion phases, $T_{\text{obs}} \sim [\dot{e}t\rho(t, v_{\text{diff}})/a]^{1/4}$ (equation 25), and $T_{\text{obs}} \sim T_0(t/t_{\text{inj}})^{-1}(v_{\text{diff}}/v_{\text{min}})^{-\xi}$ (equation 27) for the r -process and the engine models, respectively. In the transparent phase, the temperature in equations (30) and (32) are evaluated with $v = v_{\text{min}}$. Equations on observed temperature and bolometric luminosity for both models are summarized in appendix. The parameters are summarized in the first column of table 1. The set of parameters we choose here explains the observed optical and infrared light curves of GRB 130603B (see next section). The vertical dash-dotted lines in figure 3 show the time $t = t_x$ (equation 24). The diffusion radius is plotted only up to the transition time $t = t_{\text{tr}}$.

In the thick-diffusion phase, the diffusion radius ($r_{\text{diff}} \propto t^{\frac{\beta-4}{\beta-2}} = t^{-1/3}$ for $\beta = 3.5$) moves inward in the

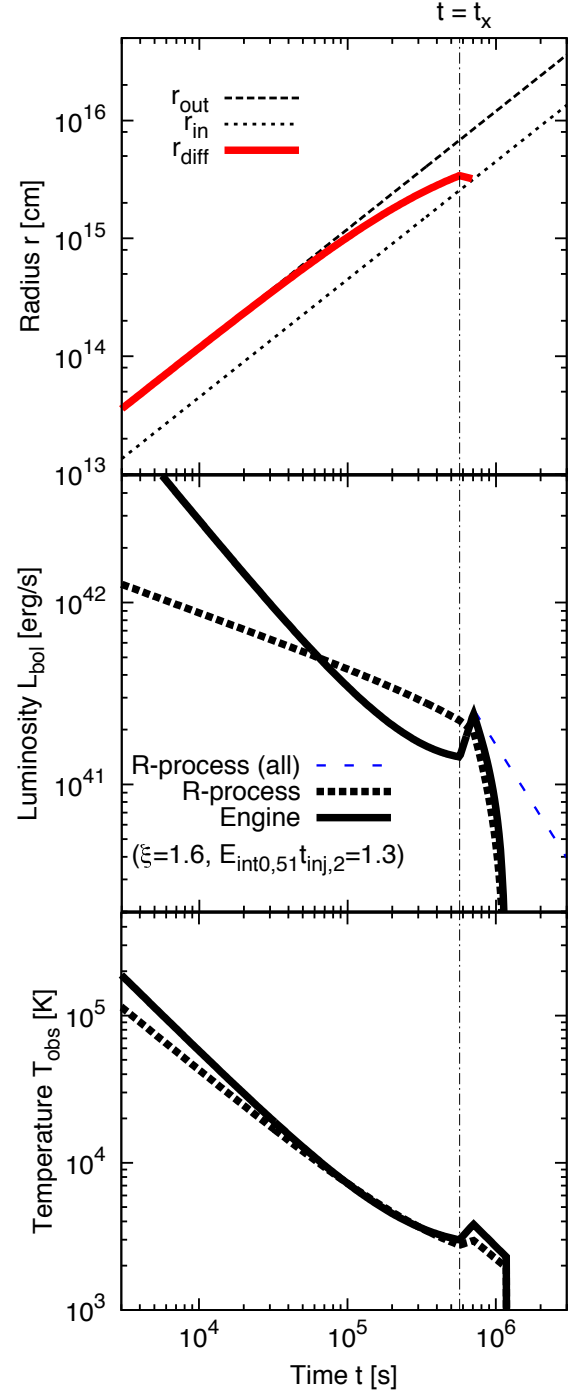


FIG. 3.— Time evolutions of the diffusion radius (top), bolometric luminosities (middle) and observed temperatures (bottom) in fiducial model (first column of table 1). Thick dashed and solid lines show the evolution for the r -process model and the engine model, respectively. For comparison, we also plot the bolometric luminosity from whole ejecta for the r -process model after the transparent phase ($t > t_{\text{tr}}$ in equation 29) as a blue long-dashed line in the middle panel.

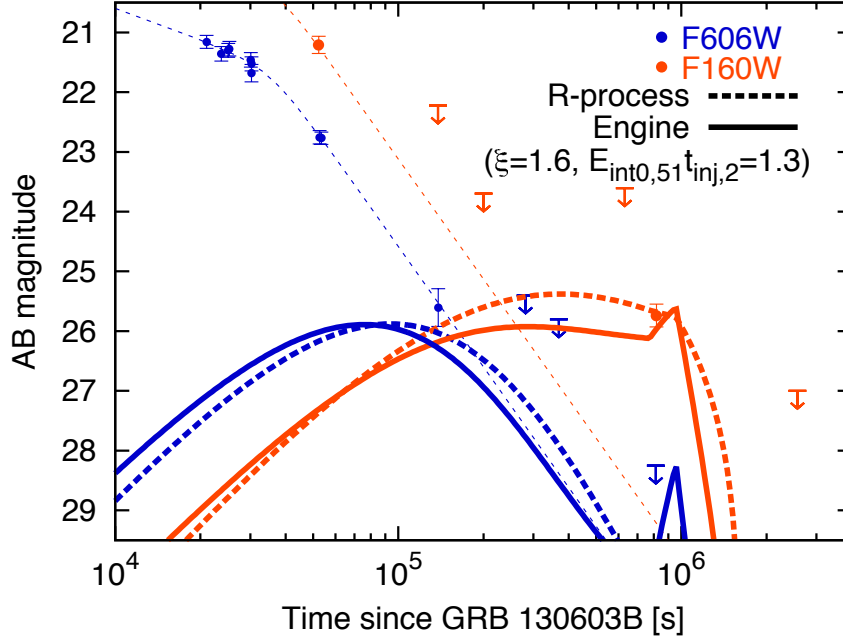


FIG. 4.— Theoretical light curves calculated under the fiducial parameter set (Table 1) at near-infrared band (F160W, red) and optical band (F606W, blue). Two models (the r -process model, solid; the engine model, dashed) are considered. The observational results of GRB 130603B ($z = 0.356$; Tanvir et al. (2013)) are also plotted. The thin dotted lines are light curves calculated from a GRB afterglow model (Tanvir et al. 2013). Both models can well reproduce the observational data.

ejecta ($r \propto t$). Since the observed luminosity and temperature are determined at the diffusion radius r_{diff} , the time evolution of luminosity and temperature strongly depends on the indices of the profile, β and ξ . For the r -process model, the bolometric luminosity decreases with time ($L_{\text{bol}} \propto t^{\frac{2(\beta-3)}{\beta-2}-\alpha} = t^{-0.633}$) in the thick-diffusion phase (see equation 26), which is more rapid than that in the thin-diffusion phase ($L_{\text{bol}} \propto t^{1-\alpha} = t^{-0.3}$, see equation 19). Since the index of the mass density $\beta = 3.5$ is close to 3, in which the mass of each shell with a certain size δr is the same value in logarithmic scale, the mass between the diffusion radius r_{diff} and its twice $2r_{\text{diff}}$ does not significantly change with time. The luminosity is mainly determined by that mass so that the evolution of the luminosity is slow compared with the evolution of nuclear heating rate ($\propto t^{-\alpha}$) in the thick-diffusion phase. On the other hand, bolometric luminosity and observed temperature increase with time in the engine model with the parameter set of the fiducial model. These mainly reflect the profile of the temperature distribution ($\xi = 1.6$). In fact, using equation (28), the index of the time t for the bolometric luminosity is $-2(\beta+1-4\xi)/(\beta-2) \sim 2.53$ for the engine model.

After the transition time $t \geq t_{\text{tr}}$, the luminosity and temperature are almost determined by the quantities at the inner edge of the ejecta. Then, the evolution of the luminosity and temperature does not significantly depend on the indices of profile β and ξ as in the case of the thin-diffusion phase (except for the case $\xi < 0.75$ of the engine model, equation 33). Since our used profile of mass density has an artificially steep cut-off at the inner edge of the ejecta (figure 2), bolometric luminosity in both models rapidly declines after the time $t \geq t_{\text{tr}}$. In the bottom panel of figure 3, the observed tempera-

ture in both models has steep cutoff at $2r_{\text{diff}} = r_{\text{in}}$. For comparison, we also consider the time evolution of bolometric luminosity from the whole ejecta $L_{\text{bol}} = M_{\text{ej}} t^{-\alpha}$ in the r -process model. Time evolution is shown in the middle panel of figure 3 as a blue long-dashed line. This luminosity evolution ($L_{\text{bol}} \propto t^{-\alpha} = t^{-1.3}$) is significantly slower than that of the engine model in the transparent phase. In section 4.4, we discuss the implication for discriminating the r -process model and the engine model using these temporal behaviors.

4. DISCUSSION

4.1. Comparison with GRB 130603B

We compare the results with the optical and infrared observations of short GRB 130603B in figure 4. The fiducial parameter set in table 1 is adopted. The r -process model and the engine model result in similar light curves at the optical and infrared bands. Both of them satisfy the observational data of GRB 130603B. Note that the detection point at F606W band at $\sim 10^5$ s is consistent with the afterglow of GRB 130603B modeled as a smoothly broken power law (blue dashed line, Tanvir et al. (2013)). We regard this detected value as an upper limit for the luminosity of emission from the ejecta. The detection point at F160W band at $\sim 10^6$ s exceeds the extrapolation of the afterglow emission (red dashed line, (Tanvir et al. 2013)) so that we regard this detected emission as a thermal radiation from the ejecta.

The range of the model parameters v_{min} and M_{ej} to satisfy the constraints obtained from the observation of GRB 130603B is shown in figure 5 as colored areas (red area for the r -process model and blue area for the engine model). Note that the red area has a completely overlap with the blue area. We fix model parameters $v_{\text{max}} =$

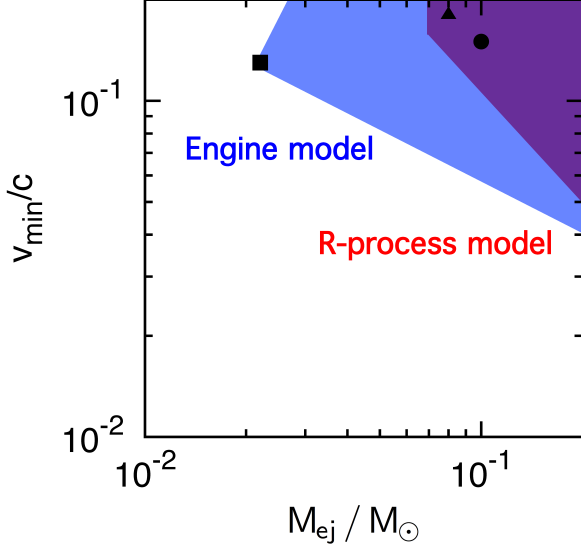


FIG. 5.— Range of parameter space in order to explain the observations of the macronova candidate, GRB 130603B (blue for the engine model and red for the r -process model). Since two regions are overlapped, the color looks like purple for the r -process model. These regions are only schematic view. We fix $v_{\max} = 0.4c$, $\beta = 3.5$, $\dot{\epsilon}_0 = 2 \times 10^{10} \text{ erg s}^{-1} \text{ g}^{-1}$ and $\alpha = 1.3$. For the opacity κ , we use the range $\kappa = 3 - 30 \text{ cm}^2 \text{ g}^{-1}$. For the engine model, we use $E_{\text{int}0}t_{\text{inj}}$ and ξ as free parameters to fit the light curve. A circle, square and triangle denote the case of the fiducial model, minimum mass model and hot interior model, respectively (see table 1).

$0.4c$, $\beta = 3.5$, $\dot{\epsilon}_0 = 2 \times 10^{10} \text{ erg s}^{-1} \text{ g}^{-1}$ and $\alpha = 1.3$ as in the fiducial model. We take into account the uncertain range of the opacity, $\kappa = 3 - 30 \text{ cm}^2 \text{ g}^{-1}$ to constraint parameters, v_{\min} and M_{ej} . In the engine model, ξ and $E_{\text{int}0}t_{\text{inj}}$ are additionally treated as free parameters to derive the allowed area in figure 5.

4.1.1. Limits on ejecta mass

In the r -process model, the luminosity becomes smaller for smaller ejecta mass M_{ej} . The small ejected mass $M_{\text{ej}} \lesssim 0.07M_{\odot}$ cannot reproduce the excess in near-infrared band detected at the follow-up observation of GRB 130603B (figure 4). The required ejecta mass is relatively large compared to the mass indicated by recent numerical simulations for a merger of binary NSs (e.g., Hotokezaka et al. (2013a); Rosswog et al. (2014); Just et al. (2014)).

In the engine model, the injected internal energy which determines the luminosity from the ejecta does not depend on the ejecta mass (except for the limit in equation 15). However, the luminosity declines rapidly after the transition time $t \gtrsim t_{\text{tr}}$ which depends on the ejecta mass as in equation (29). The condition $t_{\text{tr}} \gtrsim 10^6 \text{ s}$ in the observer frame is required to reproduce the excess observed from GRB 130603B in the near-infrared band. The condition gives the lower limit for the ejecta mass in the engine model, $M_{\text{ej}} \gtrsim 0.02M_{\odot}$ with the opacity $\kappa \sim 30 \text{ cm}^2 \text{ g}^{-1}$.

Note that the observed upper limit on the infrared luminosity at $\sim 3 \times 10^6 \text{ s}$ in the observer frame (figure 4), which corresponds to $t_{\text{tr}} \lesssim 3 \times 10^6 \text{ s}$, gives the upper limit on the ejecta mass for both models. However, this limit is not important for the range $M_{\text{ej}} < 0.2M_{\odot}$ in the

range of the opacity $\kappa = 3 - 30 \text{ cm}^2 \text{ g}^{-1}$.

4.1.2. Limits on the minimum velocity

The smaller minimum velocity v_{\min} gives the smaller bolometric luminosity at certain time in the r -process model (see equations 19 and 26). The small minimum velocity enlarges the size of ejecta (when we fix the maximum velocity v_{\max}). Then, the diffusion time t_{diff} of photons emitted from the inner region of the ejecta becomes large for the small velocity v_{\min} (equation 29). The mass between r_{diff} and $2r_{\text{diff}}$ (or r_{out}) increases toward inner region of the ejecta (as long as $\beta > 3$) so that the mass is reduced for the small minimum velocity v_{\min} at certain time. In fact, the dependence of the mass on the minimum velocity is $4\pi r_{\text{diff}}^3 \rho(t, v_{\text{diff}}) \propto v_{\min}^{\frac{\beta-3}{\beta-2}} = v_{\min}^{1/3}$. As a result, too small minimum velocity gives too small luminosity to reproduce the observed infrared excess in GRB 130603B. Moreover, the smaller minimum velocity gives the larger temperature T_{obs} at certain time (equations 25 and 30) because the mass density at the shell with small velocity is large. The difference between the detected luminosity in F160W band and the upper limit on the luminosity in F606W band at $\sim 10^6 \text{ s}$ in the observer frame gives the upper limit on the observed temperature ($T_{\text{obs}} \lesssim 4 \times 10^3 \text{ K}$). To satisfy the observed upper limit on the temperature from GRB 130603B, a lower limit of $v_{\min} \gtrsim 0.1c$ is obtained for $M_{\text{ej}} \sim 0.1M_{\odot}$.

The smaller minimum velocity v_{\min} gives higher temperature T_{obs} in the engine model (equations 27 and 32). The observational limit for the temperature at $\sim 10^6 \text{ s}$ in the observer frame indicates that the range of the minimum velocity v_{\min} is limited in the engine model ($v_{\min} \gtrsim 0.06c$ for $M_{\text{ej}} \sim 0.1M_{\odot}$).

4.1.3. Dependence on opacity

We use the temperature-independent opacity κ with the grey approximation. The r -process line opacity in general depends on frequency and changes with temperature and ionization state of the ejecta (Kasen, Badnell & Barnes 2013; Tanaka & Hotokezaka 2013). The indicated grey opacity is $\kappa = 3 - 30 \text{ cm}^2 \text{ g}^{-1}$. We discuss the dependence of the value of κ . Note that dust grains formed in low-temperature ejecta $\lesssim 2 \times 10^3 \text{ K}$ may also contribute to the total opacity (Takami, Nozawa & Ioka 2014).

In the case of the r -process model, the luminosity significantly depends on opacity κ . The larger opacity causes larger diffusion time t_{diff} so that larger time is required to observe the inner region of the ejecta for given ejecta mass M_{ej} and minimum velocity v_{\min} . In fact, two transition times t_{\times} and t_{tr} are proportional to $\kappa^{1/2}$ (equations 24 and 29). Then, the mass around the diffusion radius r_{diff} is small at certain time so that the luminosity is reduced. As a result, in order to explain the infrared excess observed in GRB 130603B, larger mass M_{ej} is required for the larger value of opacity κ . For the opacity $\kappa > 30 \text{ cm}^2 \text{ g}^{-1}$, total ejecta mass $M_{\text{ej}} \gtrsim 0.2M_{\odot}$ is required to reproduce the observed excess, which mass is much larger than the simulation results of mergers of binary NSs (e.g., Hotokezaka et al. (2013a)). On the other hand, the transition time t_{tr} is small for the small value of the opacity. Then, luminosity significantly increase at the time $\sim 10^5 \text{ s}$. For the opacity $\kappa \lesssim 3 \text{ cm}^2$

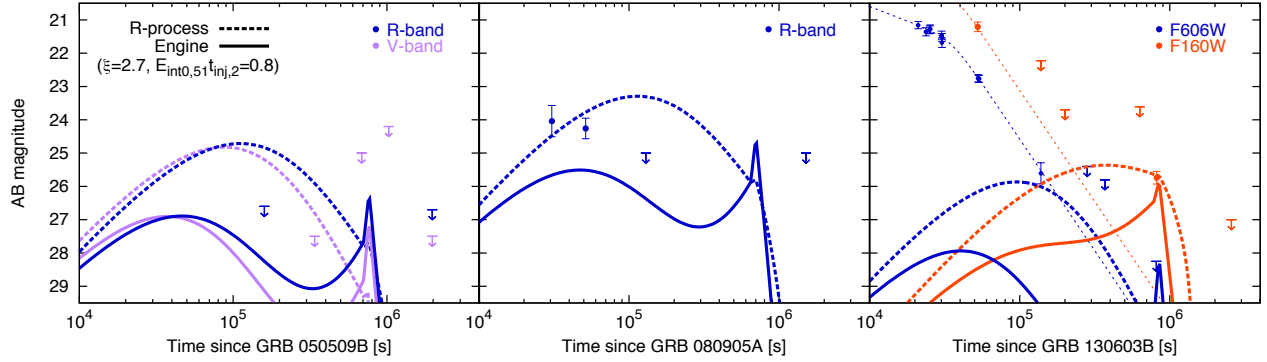


FIG. 6.— Theoretical light curves calculated under the hot interior model (table 1) at V (purple), R, F606W (blue) and F160W bands (red). Two models (the r -process model, *solid*; the engine model, *dashed*) are considered. The observational results of GRB 050509B ($z = 0.122$, Hjorth et al. (2005), left panel), GRB 080905A ($z = 0.225$, Rowlinson et al. (2010), middle panel) and GRB 130603B ($z = 0.356$, Tanvir et al. (2013), right panel) are also plotted. The engine model can well reproduce all three observational data.

g^{-1} , there is no the parameter set which gives the smaller luminosity than the detection at F606W band ($\sim 10^5$ s in the observer frame) and comparable luminosity to the observed excess at F160W band simultaneously in the r -process model.

In the case of the engine model, a larger value of opacity κ reduces the lower limit for the mass M_{ej} to explain the observed excess. For the temperature and luminosity, the opacity κ and the ejecta mass M_{ej} always degenerate in the form κM_{ej} (see equations 21, 22, 27, 28, 32 and 33). This dependence only comes from the optical depth (equation 11) because the internal energy in the ejecta does not depend on the opacity and the ejecta mass, contrary to the r -process model. We present a parameter set to give the minimum ejecta mass M_{ej} in table 1 as the minimum mass parameter set. We also plot the value of M_{ej} and v_{min} of this model in figure 5 as a square. This ejecta mass is naturally predicted by general relativistic simulations (e.g., Hotokezaka et al. (2013a)). Although the larger value of the opacity κ reduces the lower limit for the ejecta mass M_{ej} , the kinetic energy is $E_{\text{kin}} \sim 1.1 \times 10^{51}$ erg (equation 16) which is close to the initial injected energy $E_{\text{int0}} = 0.9 \times 10^{51}$ erg for the minimum mass parameter set. The lower ejecta mass M_{ej} reduces the kinetic energy of the ejecta, $E_{\text{kin}} (\propto M_{\text{ej}} v_{\text{max}}^{5-\beta} v_{\text{min}}^{\beta-3})$ in equation 16 so that the required energy E_{int0} may exceed the kinetic energy of the ejecta for the larger opacity. Therefore, the lower limit for the ejecta mass M_{ej} cannot be significantly reduced from $\sim 0.02 M_{\odot}$ even if we use the larger value of the opacity $\kappa \gtrsim 30 \text{ cm}^2 \text{ g}^{-1}$. For the small value of the opacity, larger mass and smaller minimum velocity is required to satisfy the condition $t_{\text{tr}} \gtrsim 10^6$ s ($t_{\text{tr}} \propto \kappa^{1/2} M_{\text{ej}}^{1/2} v_{\text{min}}^{-1/2}$ in equation 29). For the opacity $\kappa = 3 \text{ cm}^2 \text{ g}^{-1}$, the condition corresponds to $(M_{\text{ej}}/0.2 M_{\odot})(v_{\text{min}}/0.1c)^{-1} \lesssim 1$. Observational constraint for the temperature also requires large value of minimum velocity v_{min} . Then, there is no solution to explain the observed excess within parameter range shown in figure 5 for the opacity $\kappa = 3 \text{ cm}^2 \text{ g}^{-1}$. Therefore, for the small opacity $\kappa \leq 3 \text{ cm}^2 \text{ g}^{-1}$ the engine model cannot explain the observed excess.

4.1.4. Dependence on engine parameters

Since the engine model has additional free parameters, ξ and $E_{\text{int0}} t_{\text{inj}}$, the arrowed region of the parameters is larger than that of the r -process model. We can impose the lower limit on the parameter $E_{\text{int0}} t_{\text{inj}}$ by regarding the infrared luminosity $\sim 10^{41} \text{ erg s}^{-1}$ at $t \sim 7$ day as bolometric luminosity in the source rest frame and equation (33). The derived limit is $(E_{\text{int0}}/10^{51} \text{ erg})(t_{\text{inj}}/10^2 \text{ s}) \gtrsim 0.4$. To satisfy the optical upper limit at $\sim 10^5$ s and detected luminosity at $\sim 10^6$ s in the observer frame (figure 4), we find the lower limit on the index of the temperature profile $\xi \gtrsim 1.0$. For smaller value of the index ξ , emission from the ejecta with relatively high temperature can be observed at early time $\sim 10^5$ s so that luminosity at F606W band is larger than the observed upper limit of GRB 130603B. In addition, the smaller value of ξ decreases relative internal energy in the inner edge of the ejecta. To reproduce the luminosity at time $\sim 10^6$ s in the observer frame when observed emission comes from the inner ejecta, the smaller ξ requires the larger initial internal energy E_{int0} which exceeds the kinetic energy of the ejecta E_{kin} in some cases.

4.2. Comparison with Other GRBs with Deep Optical Observations

Several deep optical observations of short GRBs give more stringent upper limits on luminosity of macronovae than those of GRB 130603B as long as macronovae are identical (Kann et al. 2011). We compare the results with two deep optical observations of short GRBs, GRB 050509B and GRB 080905A. For the fiducial parameter set, the luminosity exceeds the observational upper limits on these two observations. In the engine model, the luminosity can significantly reduce in the early phase $\lesssim 10^5$ s without reducing the luminosity in the late phase $\sim 10^6$ s by utilizing the steep temperature profile (large ξ).

Here, we introduce the hot interior parameter set with larger value of index ξ than that of the fiducial parameter set. Since emission from the inner part of the ejecta is observed at the later time, the luminosity at the early phase when significant limits are obtained from the deep optical observations is reduced if most of the internal energy is injected to the inner part of the ejecta. We show the light curve of the hot interior parameter set in figure 6. For the hot interior parameter set, we choose

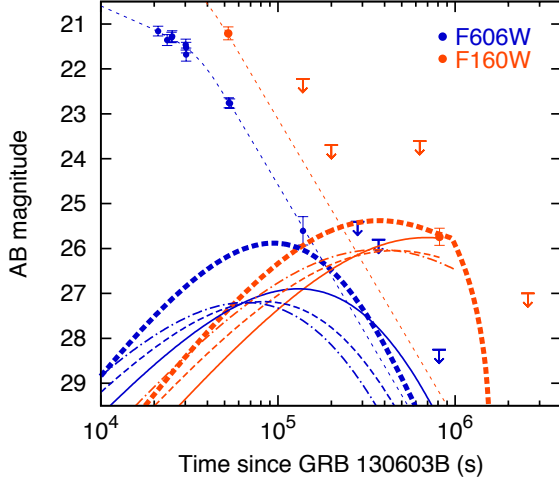


FIG. 7.— The dependence of theoretical light curves for the r -process model on the shape of the front of the ejecta. We plot for the case of GRB 130603B. Thick-dashed line denotes the fiducial model. Thin-solid, thin-dashed, and thin-dot-dashed lines correspond to the exponential profiles of mass density (equation 34) with $v'_{\max} = 0.4c, 0.5c$ and $0.6c$, respectively. We also plot the observational data from Tanvir et al. (2013).

the parameters as $M_{\text{ej}} = 0.08M_{\odot}$, $v_{\min} = 0.18c$, $t_{\text{inj}} = 10^2\text{s}$, $E_{\text{int}0} = 0.8 \times 10^{51}\text{erg}$ and $\xi = 2.7$ (the right column of table 1). From figure 6, the light curves are consistent with all three observations using the same model parameters. A possible scenario for the hot interior parameter set is that the shock produced by the activity of the central engine may not be able to catch up with the outer part of the ejecta because the velocity of the ejecta is near the light speed ($v_{\max} = 0.4c$). Then, only inner part of the ejecta will be heated. For comparison, we also show the light curves in the r -process model with the parameter set of the hot interior in figure 6 as dashed lines. The luminosity of the r -process model exceeds the observed upper limits in two observations, GRB 050509B and GRB 080905A (left and middle panels of figure 6) if we use the parameter set of the hot interior model. We are not able to find any parameter set in the r -process model, which simultaneously satisfies the observed limits from the three observations. Note that we do not argue that the r -process model is excluded from these results because we need to take into account the variations of the model parameters for each event.

4.3. Outer Region of Mass Density Profile

In the thin-diffusion phase, the light curve strongly depends on the profile of the mass density. Low mass density at the front makes the investigation of its profile difficult by numerical simulations. In order to investigate the dependence of the light curve on the mass profiles in the thin-diffusion phase, we consider other forms of the mass profile in the thin-diffusion phase and compare the light curve with that of equation (4). We adopt an exponential profile

$$\rho(t, v) = \rho_0 \left(\frac{t}{t_0} \right)^{-3} \left(\frac{v}{v_{\min}} \right)^{-\beta} \times \exp \left(- \frac{v - 0.5v_{\max}}{v'_{\max} - v} \right). \quad (34)$$

We introduce an additional free parameter $v'_{\max} (\geq v_{\max})$ and the ejecta expand $v_{\min} \leq v \leq v'_{\max}$. The calculations are the same except for $\Delta r \sim v'_{\max} t - r_{\text{diff}}$. We fix the mass with larger velocity than $0.5v_{\max}$ and calculate three models for $v'_{\max} = 0.4c, 0.5c, 0.6c$. For the other parameters, we adopt from the fiducial parameter set in table 1. We show the results in the r -process model in figure 7. Since we fix the mass with larger velocity than $0.5v_{\max}$, the bolometric luminosities near the time $t = t_{\times}$ are almost the same values. In the phase ($t \ll t_{\times}$), both the luminosity and the temperature are smaller than the fiducial model. This is because the density at the front of the ejecta is reduced in this mass profile. Since the maximum velocity effectively becomes large and the adiabatic cooling becomes efficient, these effects for the luminosity and temperature should be also seen in the engine model. We conclude that the luminosities in the phase ($t \ll t_{\times}$) have uncertainties within $\sim 1 - 2$ mag.

Note that the emission from the ejecta with the mass profile discussed here reduces the difference between the light curve in the r -process model and the upper limits of the deep optical observations (GRB 050509 and GRB 080905A) as discussed in section 4.2. Especially, the optical luminosity in the case $v'_{\max} = 0.6c$ (thin-dot-dashed line) significantly decreases after $t \gtrsim 10^5$ s. Therefore, the ejecta with relatively shallow mass distribution at the front of the ejecta is expected to explain the current optical follow-up observations in the r -process model.

4.4. Implications to Discriminate Two Models

In the fiducial parameter set, the light curves for two models in the optical and infrared bands are similar (figure 4). In figure 5, the allowed parameter region to explain the observation of GRB 130603B for both models are also overlapped. Therefore, it is difficult to discriminate two models from the currently available observational data.

In the r -process model, the light curve with mass profile $\rho \propto v^{-\beta}$ ($3 \lesssim \beta \lesssim 4$) and a parameter set which explains the infrared excess detected from GRB 130603B cannot explain the upper limits obtained from the deep optical observations of some short GRBs. Therefore, if both stringent optical upper limits for at $\sim 10^5$ s and bright infrared emission at $\sim 10^6$ s are simultaneously obtained from a single event (the difference of two magnitude $M_{\text{optical}}(\sim 10^5 \text{ s}) - M_{\text{infrared}}(\sim 10^6 \text{ s}) \gtrsim 2 \text{ mag}$), the r -process model is significantly restricted. For the engine model, these observations give a constraint for the temperature distribution, which may give new insights into the activity of the central engine.

As shown in the middle panel of figure 3, the bolometric luminosity in the r -process model from the whole ejecta (blue long-dashed line), including low temperature and/or X-rays and γ -rays produced directly in radioactive decays, more gradually declines than that for the engine model. A reason is that for the engine model, there is no energy injection after the time $t > t_{\text{inj}}$. Then, the luminosity significantly decreases when photons at the inner edge of the ejecta can diffuse out (see the middle panel of figure 3 and figure 4). The luminosity from whole ejecta can be described as $L_{\text{bol}} \sim M_{\text{ej}}\dot{\epsilon}$ in the transparent phase. The index of time t is determined by the nuclear heating rate, $\alpha \sim 1.3$. Therefore, the two models

are distinguishable by observing the temporal evolution of bolometric luminosity from the whole ejecta in this phase.

5. SUMMARY

We calculate the light curves of a macronova by developing analytical models. We model the ejecta based on the results of numerical simulations for a merger of binary NSs. In addition to the nuclear decay of r -process elements, the r -process model which is often discussed, we consider another heating mechanism for the ejecta, the engine-driven shock (engine model). We compare the results with the optical and infrared observations of the first macronova candidate associated with GRB 130603B, and show that both models can explain them. In order to reproduce the observed light curve, the r -process model requires the relatively large ejecta mass $M_{\text{ej}} \gtrsim 0.07 M_{\odot}$ which is mainly determined by the observed infrared luminosity $\sim 10^{41} \text{ erg s}^{-1}$ at $\sim 10^6 \text{ s}$. In the engine model, the internal energy of ejecta, which mainly determines the observed luminosity, does not depend on the ejecta mass. Then, unless the entire of the ejecta is effectively thin (the diffusion time is smaller than the dynamical time, $t_{\text{diff}} < t$, at the inner edge of the ejecta)⁴, the required ejecta mass is $M_{\text{ej}} \gtrsim 0.02 M_{\odot}$, which is comparable to the recent numerical simulation results. The initial internal energy E_{int0} and the injection time t_{inj} are required as $(E_{\text{int0}}/10^{51} \text{ erg})(t_{\text{inj}}/10^2 \text{ s}) \gtrsim 1$, which is consistent with the observed extended emission of short GRB, $E_{\text{iso}} \sim 10^{50} - 10^{51} \text{ erg}$ and $t_{\text{dur}} \sim 10 - 10^2 \text{ s}$. The required minimum velocity is about $v_{\text{min}} \gtrsim 0.05c$ for both models, which is mainly determined by the constraint for the observed temperature $\lesssim 4 \times 10^3 \text{ K}$ at $\sim 10^6 \text{ s}$. For the range of the opacity $\kappa \lesssim 3 \text{ cm}^2 \text{ g}^{-1}$ and $\kappa \gtrsim 30 \text{ cm}^2 \text{ g}^{-1}$, it is difficult for both models to explain the observations of macronova associated with GRB 130603B within the range $M_{\text{ej}} < 0.2 M_{\odot}$.

If macronovae are identical, the upper limits on the luminosity obtained in the deep optical observations of other short GRBs give stringent constraints on the r -process model. On the other hand, the engine model satisfies these constraints if the temperature profile is centrally concentrated in the ejecta (large ξ). Thus, if the difference between the optical magnitude M_{optical} at $\sim 10^5 \text{ s}$ and the infrared magnitude M_{infrared} at $\sim 10^6 \text{ s}$ is larger than $\sim 2 \text{ mag}$ in a single event, the r -process model is difficult to explain the observations unless the front of the ejecta has much shallow mass distribution. Another difference in the light curves between two models is the bolometric luminosity at the transparent phase when dynamical time is smaller than the diffusion time at the inner edge of the ejecta r_{in} . Although the optical and infrared luminosities rapidly decrease in the transparent phase, the bolometric luminosity from the whole ejecta, including lower frequency than near-infrared band and/or X-rays and γ -rays produced directly in radioactive decays, is determined by the energy injection rate of nuclear decay, $\dot{\epsilon} \propto t^{-\alpha}$ ($\alpha \sim 1.3$). For the engine model, the bolometric luminosity decreases rapidly in this phase

⁴ Since there is no energy injection after $t > t_{\text{inj}} \sim 10^2 \text{ s}$ in the engine model, the luminosity rapidly decreases after the time $t_{\text{tr}} \propto M_{\text{ej}}^{1/2}$ when photons can diffuse out from the inner edge of the ejecta (section 3.3).

(faster than t^{-2}). Therefore, we expect that the curve of the bolometric luminosity from the whole ejecta can distinguish between two heating mechanisms of the ejecta.

We thank K. Asano, K. Kiuchi, H. Nagakura, T. Nakamura, Y. Sekiguchi, M. Shibata for fruitful discussions. This work is supported by KAKENHI 24103006 (S.K., K.I.), 24.9375 (H.T.), 24000004, 26247042, 26287051 (K.I.).

APPENDIX A. ANALYTIC FORMULAE FOR MACRONOVA LIGHT CURVES

We summarize the formula for the observed temperature and bolometric luminosity. The detailed derivation of equations in this appendix is described in sections 2 and 3.

Since we assume that the observed luminosity and temperature approximate to the luminosity and temperature at the diffusion radius r_{diff} (section 3), we need to calculate the diffusion radius. For the dynamics of the ejecta, we assume an isotropic and homologous expansion. Then, the velocity of ejecta v is described by equation (3)

$$v \sim r/t \quad (\text{A-1})$$

where the radius r originates the central engine and the time t is measured from the time when a compact binary merges. As in section 3.4, we calculate the diffusion radius r_{diff} from the condition that the diffusion time equals the dynamical time, $t_{\text{diff}} = t$. The diffusion time is described by equation (9) as

$$t_{\text{diff}} \sim \tau \frac{\Delta r}{c}, \quad (\text{A-2})$$

where c is the speed of the light, τ is the optical depth described by equation (11) as

$$\tau = \begin{cases} \int_{r_{\text{diff}}}^{r_{\text{out}}} \kappa \rho dr & (r_{\text{diff}} > 0.5 r_{\text{out}}) \\ \int_{r_{\text{diff}}}^{2r_{\text{diff}}} \kappa \rho dr & (r_{\text{diff}} \leq 0.5 r_{\text{out}}), \end{cases} \quad (\text{A-3})$$

and Δr is the width of the diffusion region described by the equation (10) as

$$\Delta r \sim \begin{cases} r_{\text{out}} - r_{\text{diff}} & (r_{\text{diff}} > 0.5 r_{\text{out}}) \\ r_{\text{diff}} & (r_{\text{diff}} \leq 0.5 r_{\text{out}}). \end{cases} \quad (\text{A-4})$$

In the calculation of the optical depth τ , we use the spatially uniform value of the optical depth κ with grey approximation and the ejecta mass density $\rho(t, v)$ described by equation (4) as,

$$\rho(t, v) = \rho_0 \left(\frac{t}{t_0} \right)^{-3} \left(\frac{v}{v_{\text{min}}} \right)^{-\beta}, \quad (\text{A-5})$$

where ρ_0 and t_0 are normalized factors, and v_{min} is the velocity at the inner edge of the ejecta. The radius r_{out} is the radius of the outer edge of the ejecta, described by equation (6) as

$$r_{\text{out}} = v_{\text{max}} t, \quad (\text{A-6})$$

where the velocity v_{\max} is the outer edge of the ejecta. The radius at the inner edge of the ejecta r_{in} is described by equation (7) as

$$r_{\text{in}} = v_{\min} t. \quad (\text{A-7})$$

The normalized factor $\rho_0 t_0^3$ in the profile of the mass density is determined by the ejecta mass M_{ej} (in equation 5) as

$$M_{\text{ej}} = 4\pi \int_{v_{\min} t_0}^{v_{\max} t_0} \rho(t_0, v) r^2 dr. \quad (\text{A-8})$$

We consider two heating sources of the ejecta. In the r -process model, the internal energy of the ejecta is determined by the nuclear heating rate of the r -process element described in equation (13) as

$$\dot{\epsilon} = \dot{\epsilon}_0 \left(\frac{t}{1\text{day}} \right)^{-\alpha}. \quad (\text{A-9})$$

For the engine model, we assume the temperature profile of the ejecta $T(t, v)$ as a result of the activity of the central engine, described in equation (14) as

$$T(t, v) \sim T_0 \left(\frac{t}{t_{\text{inj}}} \right)^{-1} \left(\frac{v}{v_{\min}} \right)^{-\xi}, \quad (\text{A-10})$$

where T_0 is the normalized factor. This factor is determined by the injected internal energy $E_{\text{int}0}$ at the time t_{inj} , which described in equation (15) as

$$E_{\text{int}0} = 4\pi \int_{v_{\min} t_{\text{inj}}}^{v_{\max} t_{\text{inj}}} a T^4(t_{\text{inj}}, v) r^2 dr. \quad (\text{A-11})$$

The observed temperatures for the r -process model and the engine model are given as

$$T_{\text{obs}} \sim \begin{cases} \left[\frac{\dot{\epsilon} \rho(t, v_{\text{diff}})}{a} \right]^{1/4} & (r_{\text{diff}} > r_{\text{in}}) \\ \left[\frac{\dot{\epsilon} \rho(t, v_{\min})}{a} \right]^{1/4} & (0.5r_{\text{in}} < r_{\text{diff}} \leq r_{\text{in}}) \\ 0 & (r_{\text{diff}} \leq 0.5r_{\text{in}}), \end{cases} \quad (\text{A-12})$$

and as

$$T_{\text{obs}} \sim \begin{cases} T_0 \left(\frac{t}{t_{\text{inj}}} \right)^{-1} \left(\frac{v_{\text{diff}}}{v_{\min}} \right)^{-\xi} & (r_{\text{diff}} > r_{\text{in}}) \\ T_0 \left(\frac{t}{t_{\text{inj}}} \right)^{-1} & (0.5r_{\text{in}} < r_{\text{diff}} \leq r_{\text{in}}) \\ 0 & (r_{\text{diff}} \leq 0.5r_{\text{in}}), \end{cases} \quad (\text{A-13})$$

respectively. Note that we do not use the approximation $\rho(v, t) \sim \rho(v_{\max}, t)$ and $T(v, t) \sim T(v_{\max}, t)$ in the thin-

diffusion case. The bolometric luminosities for the r -process model and engine model are given as

$$L_{\text{bol}} \sim \begin{cases} 4\pi \int_{r_{\text{diff}}}^{r_{\text{out}}} \rho(v, t) \dot{\epsilon} r^2 dr & (r_{\text{diff}} > 0.5r_{\text{out}}) \\ 4\pi \int_{r_{\text{diff}}}^{2r_{\text{diff}}} \rho(v, t) \dot{\epsilon} r^2 dr & (r_{\text{in}} < r_{\text{diff}} \leq 0.5r_{\text{out}}) \\ 4\pi \int_{r_{\text{in}}}^{2r_{\text{diff}}} \rho(v, t) \dot{\epsilon} r^2 dr & (0.5r_{\text{in}} < r_{\text{diff}} \leq r_{\text{in}}) \\ 0 & (r_{\text{diff}} \leq 0.5r_{\text{in}}), \end{cases} \quad (\text{A-14})$$

and

$$L_{\text{bol}} \sim \begin{cases} 4\pi \int_{r_{\text{diff}}}^{r_{\text{out}}} \frac{a T_{\text{obs}}^4}{t} r^2 dr & (r_{\text{diff}} > 0.5r_{\text{out}}) \\ 4\pi \int_{r_{\text{diff}}}^{2r_{\text{diff}}} \frac{a T_{\text{obs}}^4}{t} r^2 dr & (r_{\text{in}} < r_{\text{diff}} \leq 0.5r_{\text{out}}) \\ 4\pi \int_{r_{\text{in}}}^{2r_{\text{diff}}} \frac{a T_{\text{obs}}^4}{t} r^2 dr & (0.5r_{\text{in}} < r_{\text{diff}} \leq r_{\text{in}}) \\ 0 & (r_{\text{diff}} \leq 0.5r_{\text{in}}), \end{cases} \quad (\text{A-15})$$

respectively. An example of the calculated result is shown in figure 3.

We present the numerical values with the parameter dependence for convenience. Unlike such as equations (24) and (29), we include the contribution from subdominant terms to the numerical values when we integrate equations. Some of the subdominant terms include the ratio v_{\max}/v_{\min} . Hereafter, the value $v_{\max}/v_{\min} = 4$ in subdominant terms are fixed and are not included to the obtained parameter dependence. We introduce the normalized quantities $M_{\text{ej},0.1} \equiv M_{\text{ej}}/0.1M_{\odot}$, $v_{\min,0.1} \equiv v_{\min}/0.1c$, $v_{\max,0.4} \equiv v_{\max}/0.4c$, $\kappa_{10} \equiv \kappa/10 \text{ cm}^2 \text{ g}^{-1}$, $E_{\text{int}0,51} \equiv E_{\text{int}0}/10^{51} \text{ erg}$ and $t_{\text{inj},2} \equiv t_{\text{inj}}/10^2 \text{ s}$. For other parameters, we fix the index of the mass density profile $\beta = 3.5$ and the parameters of the nuclear heating rate $\dot{\epsilon}_0 = 2 \times 10^{10} \text{ erg s}^{-1} \text{ g}^{-1}$ and $\alpha = 1.3$. We also introduce the normalized time $t_5 \equiv t/10^5 \text{ s}$ and $t_6 \equiv t/10^6 \text{ s}$. The values of the observed temperature and bolometric

luminosity in the thin-diffusion phase are

$$T_{\text{obs}} \sim \begin{cases} 5.63 \times 10^3 \text{ K} \\ \times M_{\text{ej},0.1}^{0.25} v_{\text{min},0.1}^{0.125} v_{\text{max},0.4}^{-0.875} t_5^{-0.825} \\ (r\text{-process}) \\ 6.72 \times 10^3 \text{ K} \\ \times E_{\text{int}0,51}^{0.25} t_{\text{inj},2}^{0.25} v_{\text{min},0.1}^{0.25} v_{\text{max},0.4}^{-1} t_5^{-1} \\ (\text{engine}, \xi = 1) \\ 2.34 \times 10^3 \text{ K} \\ \times E_{\text{int}0,51}^{0.25} t_{\text{inj},2}^{0.25} v_{\text{min},0.1}^{1.25} v_{\text{max},0.4}^{-2} t_5^{-1} \\ (\text{engine}, \xi = 2) \\ 6.77 \times 10^2 \text{ K} \\ \times E_{\text{int}0,51}^{0.25} t_{\text{inj},2}^{0.25} v_{\text{min},0.1}^{2.25} v_{\text{max},0.4}^{-3} t_5^{-1} \\ (\text{engine}, \xi = 3), \end{cases} \quad (\text{A-16})$$

and

$$L_{\text{bol}} \sim \begin{cases} 3.51 \times 10^{41} \text{ erg s}^{-1} \\ \times \kappa_{10}^{-0.5} M_{\text{ej},0.1}^{0.5} v_{\text{min},0.1}^{0.25} v_{\text{max},0.4}^{0.25} t_5^{-0.3} \\ (r\text{-process}) \\ 7.10 \times 10^{41} \text{ erg s}^{-1} \\ \times \kappa_{10}^{-0.5} M_{\text{ej},0.1}^{0.5} E_{\text{int}0,51} t_{\text{inj},2} v_{\text{min},0.1}^{0.75} v_{\text{max},0.4}^{-0.25} t_5^{-1} \\ (\text{engine}, \xi = 1) \\ 1.04 \times 10^{40} \text{ erg s}^{-1} \\ \times \kappa_{10}^{-0.5} M_{\text{ej},0.1}^{0.5} E_{\text{int}0,51} t_{\text{inj},2} v_{\text{min},0.1}^{4.75} v_{\text{max},0.4}^{-4.25} t_5^{-1} \\ (\text{engine}, \xi = 2) \\ 7.32 \times 10^{37} \text{ erg s}^{-1} \\ \times \kappa_{10}^{-0.5} M_{\text{ej},0.1}^{0.5} E_{\text{int}0,51} t_{\text{inj},2} v_{\text{min},0.1}^{8.75} v_{\text{max},0.4}^{-8.25} t_5^{-1} \\ (\text{engine}, \xi = 3), \end{cases} \quad (\text{A-17})$$

respectively.

The transition time from the thin-diffusion phase to the thick-diffusion phase t_{\times} is

$$t_{\times} = \sqrt{\frac{2^{\beta-4}(\beta-3)(1-2^{1-\beta})\kappa M_{\text{ej}}}{\pi(\beta-1)[1-(v_{\text{max}}/v_{\text{min}})^{3-\beta}]cv_{\text{max}}}} \left(\frac{v_{\text{max}}}{v_{\text{min}}}\right)^{3-\beta} \\ \sim 4.53 \times 10^5 \kappa_{10}^{0.5} M_{\text{ej},0.1}^{0.5} v_{\text{min},0.1}^{0.25} v_{\text{max},0.4}^{-0.75} \text{ s}. \quad (\text{A-18})$$

The values of the observed temperature and bolometric

luminosity in the thick-diffusion phase are

$$T_{\text{obs}} \sim \begin{cases} 3.89 \times 10^3 \text{ K} \\ \times \kappa_{10}^{-0.583} M_{\text{ej},0.1}^{-0.333} v_{\text{min},0.1}^{-0.167} t_6^{0.342} \\ (r\text{-process}) \\ 3.86 \times 10^3 \text{ K} \\ \times \kappa_{10}^{-0.667} M_{\text{ej},0.1}^{-0.667} E_{\text{int}0,51}^{0.25} t_{\text{inj},2}^{0.25} v_{\text{min},0.1}^{-0.083} t_6^{0.333} \\ (\text{engine}, \xi = 1) \\ 7.73 \times 10^3 \text{ K} \\ \times \kappa_{10}^{-1.333} M_{\text{ej},0.1}^{-1.333} E_{\text{int}0,51}^{0.25} t_{\text{inj},2}^{0.25} v_{\text{min},0.1}^{0.583} t_6^{1.667} \\ (\text{engine}, \xi = 2) \\ 1.29 \times 10^4 \text{ K} \\ \times \kappa_{10}^{-2} M_{\text{ej},0.1}^{-2} E_{\text{int}0,51}^{0.25} t_{\text{inj},2}^{0.25} v_{\text{min},0.1}^{1.25} t_6^3 \\ (\text{engine}, \xi = 3), \end{cases} \quad (\text{A-19})$$

and

$$L_{\text{bol}} \sim \begin{cases} 1.16 \times 10^{41} \text{ erg s}^{-1} \\ \times \kappa_{10}^{-0.333} M_{\text{ej},0.1}^{0.667} v_{\text{min},0.1}^{0.333} t_6^{-0.633} \\ (r\text{-process}) \\ 9.59 \times 10^{40} \text{ erg s}^{-1} \\ \times \kappa_{10}^{-0.667} M_{\text{ej},0.1}^{-0.667} E_{\text{int}0,51} t_{\text{inj},2} v_{\text{min},0.1}^{0.667} t_6^{-0.667} \\ (\text{engine}, \xi = 1) \\ 5.96 \times 10^{41} \text{ erg s}^{-1} \\ \times \kappa_{10}^{-3.333} M_{\text{ej},0.1}^{-3.333} E_{\text{int}0,51} t_{\text{inj},2} v_{\text{min},0.1}^{3.333} t_6^{4.667} \\ (\text{engine}, \xi = 2) \\ 2.62 \times 10^{42} \text{ erg s}^{-1} \\ \times \kappa_{10}^{-6} M_{\text{ej},0.1}^{-6} E_{\text{int}0,51} t_{\text{inj},2} v_{\text{min},0.1}^6 t_6^{10} \\ (\text{engine}, \xi = 3), \end{cases} \quad (\text{A-20})$$

respectively. Note that since the diffusion radius r_{diff} cannot be analytically described in the thin-diffusion phase, we use the approximations $\rho(v, t) \sim \rho(v_{\text{max}}, t)$ and $T(v, t) \sim T(v_{\text{max}}, t)$ in equations (A-16) and (A-17). These approximations make discontinuity at the transition time t_{\times} . The ratios of the temperature in the thick-diffusion phase to the temperature in the thin-diffusion phase for the r -process $A_{\text{T},r}$ and the engine model $A_{\text{T},e}$ at the time t_{\times} are

$$A_{\text{T},r} = 2^{\beta/4} \\ \sim 1.83 \quad (\text{A-21})$$

and

$$A_{\text{T},e} = 2^{\xi} \\ \sim \begin{cases} 2.00 & (\xi = 1) \\ 4.00 & (\xi = 2) \\ 8.00 & (\xi = 3), \end{cases} \quad (\text{A-22})$$

respectively. The ratios of the luminosity in the thick-diffusion phase to the luminosity in the thin-diffusion phase for the r -process model $A_{\text{L},r}$ and the engine model $A_{\text{L},e}$ at the time t_{\times} are

$$A_{\text{L},r} = 2^{\frac{\beta-4}{2}} \left(\frac{1-2^{3-\beta}}{\beta-3} \right) \sqrt{\frac{\beta-1}{1-2^{1-\beta}}}$$

$$\sim 0.858 \quad (\text{A-23}) \quad \text{and}$$

and

$$A_{L,e} = 2^{\frac{-\beta-4+8\xi}{2}} \left(\frac{1-2^{3-4\xi}}{4\xi-3} \right) \sqrt{\frac{\beta-1}{1-2^{1-\beta}}} \quad (\text{A-24})$$

$$\sim \begin{cases} 1.04 & (\xi = 1) \\ 6.42 & (\xi = 2) \\ 58.8 & (\xi = 3), \end{cases}$$

respectively.

The transition time from the thick-diffusion phase to the transparent phase t_{tr} is

$$t_{tr} = \sqrt{\frac{(\beta-3)(1-2^{1-\beta})\kappa M_{ej}}{4\pi(\beta-1)[1-(v_{\max}/v_{\min})^{3-\beta}]cv_{\min}}} \quad (\text{A-25})$$

$$\sim 7.62 \times 10^5 \kappa_{10}^{0.5} M_{ej,0.1}^{0.5} v_{\min,0.1}^{-0.5} \text{ s.}$$

We introduce another transition time t_{tr2} when the upper limit of the integral for the luminosity $2r_{\text{diff}}$ reaches the inner edge of the ejecta r_{in} ,

$$t_{tr2} = 2^{\frac{\beta-2}{2}} t_{tr} \quad (\text{A-26})$$

$$\sim 1.28 \times 10^6 \kappa_{10}^{0.5} M_{ej,0.1}^{0.5} v_{\min,0.1}^{-0.5} \text{ s.}$$

The values of the observed temperature and bolometric luminosity in the transparent phase ($t_{tr} \leq t < t_{tr2}$) are

$$T_{\text{obs}} \sim \begin{cases} 2.83 \times 10^3 \text{ K} \\ \times M_{ej,0.1}^{0.25} v_{\min,0.1}^{-0.75} t_6^{-0.825} \\ (r - \text{process}) \\ 2.69 \times 10^3 \text{ K} \\ \times E_{\text{int}0,51}^{0.25} t_{\text{inj},2}^{0.25} v_{\min,0.1}^{-0.75} t_6^{-1} \\ (\text{engine, } \xi = 1) \\ 3.74 \times 10^3 \text{ K} \\ \times E_{\text{int}0,51}^{0.25} t_{\text{inj},2}^{0.25} v_{\min,0.1}^{-0.75} t_6^{-1} \\ (\text{engine, } \xi = 2) \\ 4.33 \times 10^3 \text{ K} \\ \times E_{\text{int}0,51}^{0.25} t_{\text{inj},2}^{0.25} v_{\min,0.1}^{-0.75} t_6^{-1} \\ (\text{engine, } \xi = 3) \end{cases} \quad (\text{A-27})$$

$$L_{\text{bol}} \sim \begin{cases} 3.30 \times 10^{41} \text{ erg s}^{-1} \\ \times M_{ej,0.1} t_6^{-1.3} \left[1 - \left(\frac{t}{t_{tr2}} \right)^{0.667} \right] \\ (r - \text{process}) \\ 1.33 \times 10^{41} \text{ erg s}^{-1} \\ \times E_{\text{int}0,51} t_{\text{inj},2} t_6^{-2} \left[1 - \left(\frac{t}{t_{tr2}} \right)^{1.333} \right] \\ (\text{engine, } \xi = 1), \\ 1.00 \times 10^{41} \text{ erg s}^{-1} \\ \times E_{\text{int}0,51} t_{\text{inj},2} t_6^{-2} \left[1 - \left(\frac{t}{t_{tr2}} \right)^{6.667} \right] \\ (\text{engine, } \xi = 2), \\ 1.00 \times 10^{41} \text{ erg s}^{-1} \\ \times E_{\text{int}0,51} t_{\text{inj},2} t_6^{-2} \left[1 - \left(\frac{t}{t_{tr2}} \right)^{12} \right] \\ (\text{engine, } \xi = 3), \end{cases} \quad (\text{A-28})$$

respectively.

REFERENCES

- Aasi, J., Abadie, J., Abbott, B. P., et al. 2014, *ApJS*, 211, 7
- Abadie, J., Abbott, B. P., Abbott, R., et al. 2010a, *NIMPA*, 624, 223
- Abadie, J., Abbott, B. P., Abbott, R., et al. 2010b, *CQG*, 27, 173001
- Acernese, F., Agathos, M., Agatsuma, K., et al. 2014, *arXiv:1408.3978*
- Arnett, W. D. 1980, *ApJ*, 237, 541
- Barnes, J., & Kasen, D. 2013, *ApJ*, 775, 18
- Barthelmy, S. D., Canniozzo, J. K., Gehrels, N., et al. 2005, *ApJ*, 635, L133
- Berger, E., Fong, W., & Chornock, R. 2013, *ApJ*, 774, L23
- Deaton, M. B., Duez, M. D., Foucart, F., O'Connor, E., Ott, C. D., Kidder, L. E., Muhlberger, C. D., Scheel, M. A., & Szilágyi, B. 2013, *ApJ*, 776, 47
- Dessart, L., Ott, C. D., Burrows, A., Rosswog, S., & Livne, E. 2009, *ApJ*, 690, 1681
- Essick, R., Vitale, S., Katsavounidis, E., Vedovato, G., & Klimentenko, S. 2014, *arXiv:1409.2435*
- Fan, Y.-Z., Yu, Y.-W., Xu, D., Jin, Z.-P., Wu, X.-F., Wei, D.-M. & Zhang, B. 2013, *ApJ*, 779, L25
- Fernández, R., Kasen, D., Metzger, B. D., & Quataert, E. 2014, *arXiv:1409.4426*
- Fernández, R., & Metzger, B. D. 2013, *MNRAS*, 435, 502
- Foucart, F., Deaton, M. B., Duez, M. D., Kidder, L. E., MacDonald, I., Ott, C. D., Pfeiffer, H. P., Scheel, M. A., Szilágyi, B., & Teukolsky, S. A. 2013, *PhRvD*, 87, 084006
- Foucart, F., Deaton, M. B., Duez, M. D., O'Connor, E., Ott, C. D., Haas, R., Kidder, L. E., Pfeiffer, H. P., Scheel, M. A., & Szilágyi, B. 2014, *PhRvD*, 90, 024026
- Grossman, D., Korobkin, O., Rosswog, S., & Piran, T. 2014, *MNRAS*, 439, 757
- Hjorth, J., Sollerman, J., Gorosabel, J., et al. 2005, *ApJ*, 630, L117
- Hotokezaka, K., Kiuchi, K., Kyutoku, K., Okawa, H., Sekiguchi, Y., Shibata, M., & Taniguchi, K. 2013a, *PhRvD*, 87, 024001
- Hotokezaka, K., Kyutoku, K., Tanaka, M., Kiuchi, K., Sekiguchi, Y., Shibata, M., & Wanajo, S. 2013b, *ApJ*, 778, L16
- Ioka, K., Kobayashi, S., & Zhang, B. 2005, *ApJ*, 631, 429
- Jin, Z.-P., Xu, D., Fan, Y.-Z., Wu, X.-F., & Wei, D.-M. 2013, *ApJ*, 775, L19
- Just, O., Bauswein, A., Ardevol Pulpillo, R., Goriely, S., & Janka, H.-T. 2014, *arXiv:1406.2687*
- Kann, D. A., Klose, S., Zhang, B., et al. 2011, *ApJ*, 734, 96
- Kasen, D., Badnell, N. R., & Barnes, J. 2013, *ApJ*, 774, 25
- Kiuchi, K., Kyutoku, K., Sekiguchi, Y., Shibata, M., & Wada, T. 2014, *PhRvD*, 90, 041502(R)
- Kiuchi, K., Kyutoku, K., & Shibata, M. 2012, *PhRvD*, 86, 064008
- Korobkin, O., Rosswog, S., Arcones, A., & Winteler, C. 2012, *MNRAS*, 426, 1940
- Kulkarni, S. R. 2005, *astro-ph/0510256*
- Kuroda, K., et al. 2010, *CQGra*, 27, 084004
- Kyutoku, K., Ioka, K., & Shibata, M. 2013, *PhRvD*, 88, 041503(R)
- Kyutoku, K., Ioka, K., & Shibata, M. 2014, *MNRAS*, 437, L6
- Kyutoku, K., Okawa, H., Shibata, M., & Taniguchi, K. 2011, *PhRvD*, 84, 064018
- Lattimer, J. M., & Schramm, D. N. 1974, *ApJ*, 192, L145
- Li, L.-X., & Paczyński, B. 1998, *ApJ*, 507, L59
- Lovelace, G., Duez, M. D., Foucart, F., Kidder, L. E., Pfeiffer, H. P., Scheel, M. A., & Szilágyi, B. 2013, *CQG*, 30, 135004
- Metzger, B. D., Bauswein, A., Goriely, S., & Kasen, D. 2014, *arXiv:1409.0544*
- Metzger, B. D., & Berger, E. 2012, *ApJ*, 746, 48
- Metzger, B. D., Martínez-Pinedo, G., Darbha, S., et al. 2010, *MNRAS*, 406, 2650
- Nagakura, H., Hotokezaka, K., Sekiguchi, Y., Shibata, M., & Ioka, K. 2014, *ApJ*, 784, L28
- Nakamura, T., Kashiya, K., Nakauchi, D., Suwa, Y., Sakamoto, T., & Kawai, N. 2013, *arXiv:1312.0297*
- Nakar, E., & Piran, T. 2011, *Nature*, 478, 82
- Nakar, E., & Sari, R. 2010, *ApJ*, 725, 904
- Narayan, R., Paczyński, B., & Piran, T. 1992, *ApJ*, 395, L83
- Piran, T., Korobkin, O., & Rosswog, S. 2014, *arXiv:1401.2166*
- Piran, T., Nakar, E., & Rosswog, S. 2013, *MNRAS*, 430, 2121
- Popov, D. V. 1993, *ApJ*, 414, 712
- Roberts, L. F., Kasen, D., Lee, W. H., & Ramirez-Ruiz, E. 2011, *ApJ*, 736, L21
- Rosswog, S. 2007, *MNRAS*, 376, L48
- Rosswog, S., Korobkin, O., Arcones, A., Thielemann, F.-K., & Piran, T. 2014, *MNRAS*, 439, 744
- Rosswog, S., Liebendörfer, M., Thielemann, F.-K., Davies, M. B., Benz, W., & Piran, T. 1999, *A&A*, 341, 499
- Rowlinson, A., Wiersema, K., Levan, A. J., et al. 2010, *MNRAS*, 408, 383
- Ruffert, M., & Janka, H.-T. 2001, *A&A*, 380, 544
- Rybicki, G. B., & Lightman, A. P. 1979, *Radiative Processes in Astrophysics* (New York: Wiley)
- Sakamoto, T., Barthelmy, S. D., Baumgartner, W. H., et al. 2011, *ApJS*, 195, 2
- Sakurai, A. 1960, *Commun. Pure Appl. Math.*, 13, 353
- Shibata, M., Suwa, Y., Kiuchi, K., & Ioka, K. 2011, *ApJ*, 734, L36
- Takami, H., Kyutoku, K., & Ioka, K. 2014, *PhRvD*, 89, 063006
- Takami, H., Nozawa, T., & Ioka, K. 2014, *ApJ*, 789, L6
- Tanaka, M., & Hotokezaka, K. 2013, *ApJ*, 775, 113
- Tanvir, N. R., Levan, A. J., Fruchter, A. S., Hjorth, J., Hounsell, R. A., Wiersema, K., & Tunnicliffe, R. L. 2013, *Nature*, 500, 547
- Wanajo, S., Sekiguchi, Y., Nishimura, N., Kiuchi, K., Kyutoku, K., & Shibata, M. 2014, 789, L39